
Flow Mismatching: Unsupervised Anomaly Detection via Velocity Discrepancies in Flow Matching Models

Shengzhe Chen¹ Mehrdad Moradi² Kamran Paynabar² Hao Yan¹
 schen415@asu.edu mmoradi6@gatech.edu kamran.paynabar@isye.gatech.edu haoyan@asu.edu
¹Arizona State University
²Georgia Institute of Technology

Abstract

We propose Flow Mismatching, an unsupervised anomaly detection method that deliberately avoids reconstruction-based paradigms. Instead, we treat flow matching as geometric dynamics and leverage a key insight: anomalies occur at places where the learned normal flow disagrees with the geometric path toward a test image.

Given a flow matching model trained only on normal images, we probe its learned velocity field along affine paths from Gaussian noise to a target image. Along each path, we compare the model-predicted velocity, which follows normal generative dynamics, with the geometric velocity toward the target, which includes any anomalous content. Anomalies induce strong local disagreement between these velocities. Aggregating the mismatch over different time steps and multiple paths yields pixel-wise heatmaps and image-level scores without test-time optimization, feature memories, or additional calibration.

Our analysis shows that the population mismatch decomposes into an irreducible denoising term and a Fisher-divergence term between the test-path and normal-path score functions, which identifies the score-gap component that drives anomaly separation and explains the effectiveness of robust path aggregation. Extensive experiments on MVTec-AD and VisA demonstrate superior performance compared with SOTA reconstruction-based and recent flow matching-based approaches.

1 Introduction

Industrial visual anomaly detection aims to identify subtle manufacturing defects, where anomalies are rare, diverse, and expensive to miss. In this setting, training data typically contains only normal samples, requiring unsupervised methods that can detect and localize anomaly at test time.

Existing methods and limitations. Unsupervised anomaly detection methods are commonly reconstruction-based, feature-based, or score-based. Reconstruction methods, including GANs, autoencoders, and diffusion models, detect anomalies through reconstruction residuals, but may also reconstruct plausible defects and weaken the anomaly signal. Feature-based methods compare test features with normal prototypes, often relying on memory banks, patch retrieval, or separate feature extractors. Score-based methods estimate likelihoods or score functions, but may require expensive inference-time gradient computation. These limitations motivate a direct test-time signal that avoids explicit reconstruction, external feature memories, and back-propagation at inference.

Flow matching as normal feature dynamics. Flow matching [Lipman et al., 2023] learns a continuous-time generative model by regressing a deterministic velocity field that transports samples from a simple Gaussian prior to the data distribution. When trained on normal data only, it encodes normal sample manifold and defines a “normal” generative dynamics. Therefore, normal flow velocity has the inherent ability in separating anomalies by incorporating the following insight:

Anomalies reveal themselves as velocity disagreement. Our key insight is that *anomalies occur at places where the learned normal flow velocity disagrees with the geometric path velocity to the test image*. In detection, we construct affine paths from random Gaussian noise to a possibly anomalous target image. Along each path, we compare the two velocities: the model-predicted velocity, which follows normal generative dynamics, and the geometric path velocity toward the target, which potentially includes anomalous content. When the test image contains anomalies, the two velocities diverge strongly in anomalous regions, while remaining aligned on normal regions. Building on this signal, we propose **Flow Mismatching**: a test-time detector that aggregates per-pixel velocity discrepancies over multiple paths to produce anomaly heatmaps and image-level scores using only forward passes, without auxiliary components like memory-bank or pretrained feature extractor.

Theoretical guarantees. Our analysis formalizes that the velocity mismatch signal decomposes into two interpretable terms: a denoising error that captures irreducible uncertainty, and a Fisher-divergence term between the test-path distribution and the normal-path distribution. The latter quantifies how much the score function induced by the test-conditioned paths deviates from that of normal paths, explaining why velocity mismatch separates defects. We then provide a concise quantile bridge bound that motivates robust path aggregation.

Our contributions are threefold. **(1) Method.** We propose *Flow Mismatching*, a purely test-time detector that computes per-pixel velocity discrepancy between a flow matching model trained on normal data and geometric transport direction, aggregating time steps and multiple paths to produce anomaly heatmaps and image-level anomaly scores. **(2) Theory.** We show that the mismatch signal decomposes into a denoising term and a Fisher-divergence term between score functions, yielding a principled separation mechanism. **(3) Empirics.** On MVTEC-AD and VisA, *Flow Mismatching* with U-Net architecture matches or even outperforms reconstruction-based baselines that rely on advanced architectures like Mamba or powerful pretrained feature extractors like ViT and DINO, and surpasses flow-matching-based AD methods. It also provides a tunable test-time compute mechanism: a small number of paths and time steps along each path gives high-throughput detection, while larger budgets improve detection performance and robustness through parallelizable forward passes.

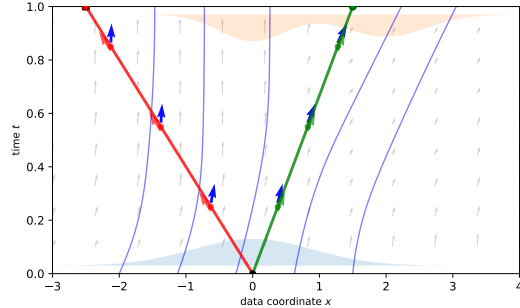


Figure 1: Velocity mismatch in the (x, t) plane. Light arrows denote the learned flow $v_\theta(x, t)$ from prior to normal data, while colored affine paths from the same x_0 target either a normal sample (green) or an anomalous sample (red). At selected times, the predicted velocity $v_\theta(x_t, t)$ aligns with the geometric velocity $y - x_0$ for normal targets but disagrees for anomalous targets, revealing the anomaly signal.

2 Related Works

2.1 Industrial Visual Anomaly Detection

Unsupervised industrial visual anomaly detection aims to learn the distribution of normal samples and identify deviations at test time. A major line of work follows the reconstruction paradigm. A model is trained to reconstruct normal images, and anomalies are detected from reconstruction errors. Early GAN- and autoencoder-based methods improve this principle through stronger normal-pattern modeling and feature localization [Alzarooni et al., 2025]. More recent reconstruction-based approaches further strengthen this paradigm with powerful visual backbones, including Dino-based [Caron et al., 2021] feature modeling in Dinomaly [Guo et al., 2025], Mamba-based Gu and Dao [2023] sequence/state-space modeling in MambaAD [He et al., 2024b], and ViT-based [Dosovitskiy et al., 2021] reconstruction in ViTAD [Zhang et al., 2025b].

More recently, diffusion and score-based models have been used for anomaly detection. DiffusionAD [Zhang et al., 2025a] formulates anomaly detection as one-step noise-to-normal reconstruction and reports strong results. TransFusion [Fučka et al., 2024] introduces transparency-guided diffusion for defect localization, while HDM [Weng et al., 2025] unifies diffusion-based generation and discrimination in a single framework. To reduce inference latency, SR-DM [Wang et al., 2024]

adopts an implicit diffusion formulation for efficient industrial deployment. Beyond direct detection, diffusion models have also been used for defect synthesis and data augmentation. DDPM-MoCo [He et al., 2024c] combines diffusion-based generation with contrastive learning, and [Xu et al., 2025] explores training-free defect generation with pre-trained diffusion models.

2.2 Flow-Matching-Based Anomaly Detection

Flow Matching (FM) [Lipman et al., 2023] provides a geometric view of generative modeling by learning a time-dependent velocity field that transports a standard Gaussian prior p_0 to the data distribution p_1 . FM learns a velocity field $v_\theta(x, t)$ whose ODE

$$\frac{dx_t}{dt} = v_\theta(x_t, t), \quad t \in [0, 1], \quad \mathcal{L}_{\text{CFM}}(\theta) = \mathbb{E}_{x_0, x_1, t} \left[\|v_\theta(x_t, t) - (x_1 - x_0)\|_2^2 \right], \quad (1)$$

pushes samples from $x_0 \sim p_0$ toward $x_1 \sim p_1$. In conditional flow matching, one samples pairs $(x_0, x_1) \sim (p_0, p_1)$ and defines a tractable affine interpolation path $x_t = (1 - t)x_0 + tx_1$ with target velocity $x_1 - x_0$. The training objective \mathcal{L}_{CFM} then becomes velocity regression. When trained only on normal images, the learned field describes normal generative dynamics. This makes FM naturally suitable for anomaly detection through vector-field diagnostics.

Existing FM-based anomaly detection methods differ mainly in how they use the learned flow. One direction modifies the flow direction or training objective. WT-Flow [Li et al., 2025a] studies time-reversed flow matching, transporting data toward noise for density estimation, and introduces Worst Transport regularization to address non-invertibility of linear paths in high dimensions. Another direction uses FM as a correction mechanism. Reflect [Beizae et al., 2025] transports anomalous latent codes toward the normal distribution and detects defects by comparing the original image with its corrected version. D-Flow [Ben-Hamu et al., 2024] searches for a closest generated sample under a given condition, which is powerful but requires solving an expensive test-time inverse problem.

Several recent works also support the use of velocity-based signals for anomaly detection. TCCM [Li et al., 2025b] detects tabular anomalies by measuring one-step deviation from a contraction path, while It’s not a FAD [Vaselli et al., 2025] uses simplified velocity-norm metrics for real-time anomaly detection in high-energy physics. From a theoretical perspective, the Energy-Tweedie identity [Leban, 2025] connects path derivatives of energy scores with noisy marginal scores, further suggesting that velocity fields encode information about the underlying data score.

3 Flow Mismatching Anomaly Detection Method

Problem Setup. We assume access to a training set of images from p_{data} , representing the distribution of normal (anomaly-free) samples. A conditional flow matching model $v_\theta(x, t)$ is trained on the normal data, learning a velocity field of the dynamics from a standard Gaussian prior $\mathcal{N}(0, I)$ to p_{data} . At test time, given a possibly anomalous target image y , our goal is to produce a pixel-wise anomaly heatmap H for anomaly localization and an image-level anomaly score S .

Single path velocity discrepancy. Given the target image y to be evaluated and a random $x_0 \sim \mathcal{N}(0, I)$ from the Gaussian prior, we define a deterministic interpolation path x_t and the *geometric velocity* g (conditioned on the target image y) as the time derivative:

$$x_t = (1 - t)x_0 + ty, \quad t \in [0, 1], \quad g(x_0, y, t) = y - x_0 = \frac{d}{dt}x_t. \quad (2)$$

When y contains anomalies, at any intermediate point x_t along the path, the geometric velocity g attempts to reproduce the anomaly in y , while the learned flow $v_\theta(x_t, t)$ seeks to generate normal features. Thus, in anomalous regions, the two velocities disagree significantly, while in normal regions they align well. This key insight is visualized in Figure 3, which shows how the velocity mismatch distinguishes normal from abnormal samples. The per-pixel squared discrepancy $\|v_\theta(x_t, t)(i) - g(x_0, y, t)(i)\|_2^2$ naturally serves as an indicator of anomaly at pixel i . The ℓ_2 norm is taken over the channel dimension (each velocity vector at pixel i is 3-dimensional due to RGB channel). We use squared norms to maintain consistency with our theoretical analysis (see Section 4).

Aggregation of paths. Because $v_\theta(x_t, t)$ depends on the stochastic x_0 , an individual path may introduce variability or spurious responses. For robustness, we sample K independent Gaussian

seeds, $\mathcal{X} = \{x_0^1, x_0^2, \dots, x_0^K\}$, $x_0^k \sim \mathcal{N}(0, I)$. For each seed $k \in [K]$, we define a deterministic path $x_t^k = (1-t)x_0^k + ty$ with geometric velocity $g^k = y - x_0^k$. For each pixel p and time t , we compute per-path squared discrepancies and aggregate the K paths via a *path aggregator* \mathcal{A} :

$$Z_t^{(k)}(i) = \|v_\theta(x_t^k, t)(i) - g^k(i)\|_2^2, \quad \delta_t(i) = \mathcal{A}(\{Z_t^{(k)}(i)\}_{k \in [K]}). \quad (3)$$

Common choices include: (1) *Minimum* $\delta_t^{\min}(i) = \min_{k \in [K]} Z_t^{(k)}(i)$, which acts as consensus voting so that only pixels consistently anomalous across paths retain high scores, reducing false positives (see Remark 4.5). (2) *Average* $\delta_t^{\text{avg}}(i) = \frac{1}{K} \sum_{k=1}^K Z_t^{(k)}(i)$, which is unbiased for $\mathbb{E}[Z_t(i)]$. (3) α -*percentile* $\delta_t^{(\alpha)}(i) = Z_{t, (\lceil \alpha K \rceil)}(i)$ (the $\lceil \alpha K \rceil$ -th order statistic), which interpolates between minimum and average and offers exponential tail control. Our theory (Section 4) analyzes the velocity discrepancy term under quantile operators and provides statistical guarantees for the aggregators.

Time discretization and weighting. We discretize the time interval $(0, 1)$ using T evenly spaced interior times $\mathcal{T} = \left\{ \frac{j}{T+1} : j = 1, \dots, T \right\}$, which excludes the endpoints $t = 0$ and $t = 1$ for numerical stability. At $t = 0$, the predicted flow velocity has no connection to y since x_0 is independent of y . At $t = 1$, the path collapses to $x_t = y$ while the affine-path velocity target still depends on the unobserved seed x_0 , and score identities become ill-conditioned; we therefore omit $t = 1$ in implementation (Appendix A.7 explains how this numerical degeneracy is distinct from the population theory, where the weighted denoising contribution stays bounded as $t \uparrow 1$).

The final pixel-level *anomaly heatmap* and image-level *anomaly score* are computed as:

$$H(i) = \frac{1}{|\mathcal{T}|} \sum_{t \in \mathcal{T}} w(t) \delta_t(i), \quad S = \max_{i \in \Omega} H(i) + \frac{1}{|\Omega_{\text{topn}}|} \sum_{i \in \Omega_{\text{topn}}} H(i), \quad (4)$$

where $w(t) = t^2$ is a time-dependent weight function. Proposition 4.4 shows that the choice of $w(t)$ arises naturally from variance-weighted loss in y -space, which translates to t^2 on velocity residuals after accounting for the $(1-t)^2$ scaling factor. Ω denotes the pixel domain, and Ω_{topn} denotes the set of pixels corresponding to the top 1% of values in the heatmap H .

Adjustable test-time compute: path/time scaling. Flow Mismatching exposes an explicit test-time compute knob: K controls path-wise robustness and T controls multi-noise-scale evidence. Unlike reconstruction or inverse-optimization methods, increasing compute only requires additional forward passes, which are parallelizable across paths. This gives a flexible detector: low K, T for high-throughput processing and larger K, T for accuracy-critical inspection. The computational complexity is $O(KT)$ evaluations of v_θ per image. Reasons for aggregating over multiple paths and time steps are discussed in Section 4. In short, scaling up K and T improves statistical reliability of the velocity mismatch signal. Appendix B.1 provides a controlled half-moon toy setup and visualizes how increasing T and K improves stability and smoothness of the anomaly score maps. Figure 2 shows the trade-off curves of performance metrics and FPS.

Empirical ablation confirms that accuracy improves with increased test-time compute, while modest K, T still yield reasonable results.

4 Theory: Why Flow Mismatching Works

We now provide a rigorous theoretical foundation for Flow Mismatching. Our analysis establishes formal guarantees on how velocity mismatches distinguish normal from anomalous samples. The goal is to understand the population-level anomaly score that underlies our method. The population score is defined as:

$$\mathcal{S}(y) := \int_0^1 w(t) \mathbb{E}_{x_0} \left[\|v_\theta(x_t, t) - (y - x_0)\|_2^2 \right] dt, \quad (5)$$

where $x_t = (1-t)x_0 + ty$, $x_0 \sim \mathcal{N}(0, I)$, and $w(t)$ is a time-dependent weight function. This is the continuous-time analogue of the discrete heatmap $H(i)$ defined in Equation (4) from Section 3, both aggregate squared velocity residuals $\|v_\theta(x_t, t) - (y - x_0)\|_2^2$. Our main population guarantee is Theorem 4.3, which corresponds to this weighted mismatch and relates it to denoising error and Fisher divergence via Proposition 4.1.

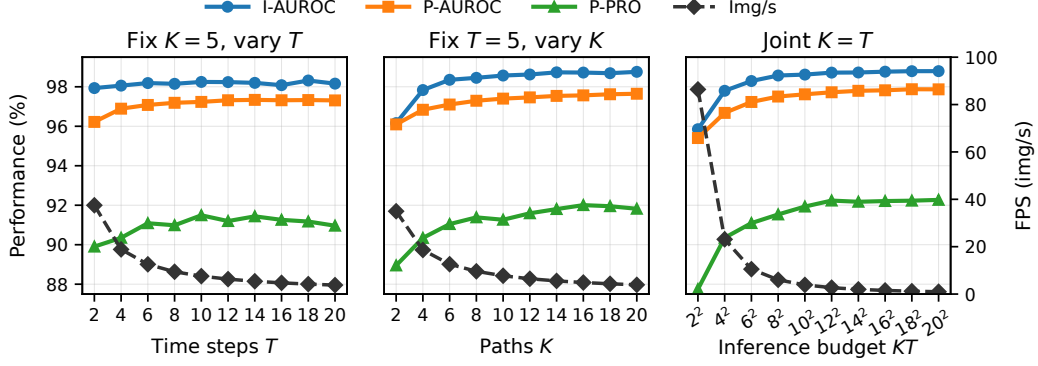


Figure 2: Accuracy–speed trade-offs under varying numbers of paths K and time steps T .

4.1 Oracle marginal velocity and learned flow velocity

Fix $t \in (0, 1)$ and consider $x_0 \sim \mathcal{N}(0, I)$ independent of $y \sim p$, where p denotes normal data distribution, with path $x_t^{(0)} := (1 - t)x_0 + ty$. Define the *oracle marginal velocity* under p :

$$v_p(t, x) := \mathbb{E}_p[y - x_0 \mid x_t^{(0)} = x],$$

which represents the expected velocity field that would transport from the prior toward normal data. As established in Section 2.2, conditional flow matching (CFM) regresses this conditional expectation by minimizing $\mathcal{L}_{\text{CFM}}(\theta) = \mathbb{E}_{x_0, y, t}[\|v_\theta(x_t, t) - (y - x_0)\|_2^2]$ over training pairs $(x_0, y) \sim (p_0, p)$.

Guaranteed by [Zhou and Liu, 2025], when trained well on normal data, the learned flow velocity satisfies $v_\theta(x, t) \approx v_p(t, x)$, approximating the oracle marginal velocity along normal paths within small enough approximation error. Thus, our anomaly signal can be viewed as the mismatch between the oracle marginal velocity and the test-conditioned geometric velocity.

The following identity further shows that the oracle velocity residual $\|v_p(t, x) - (y - x_0)\|_2^2$ directly measures the deviation from the normal posterior mean, i.e. the residual $\|y - \mu_p(x_t)\|_2$:

Proposition 4.1 (Deterministic link between y -residual and velocity residual). *Assume $x_t^{(0)} = (1 - t)x_0 + ty$. Define $\mu_p(x) := \mathbb{E}_p[y \mid x_t^{(0)} = x]$. Then for $x = x_t^{(0)}$, $y - \mu_p(x) = (1 - t)((y - x_0) - v_p(t, x))$, and hence $\|y - \mu_p(x)\|_2^2 = (1 - t)^2\|v_p(t, x) - (y - x_0)\|_2^2$.*

Proof. See Appendix A.2. □

4.2 Population mismatch decomposition

We first state an affine-path lemma used below, and then state our population decomposition for the *weighted velocity mismatch*, the detector-facing quantity aligned with the CFM training target and with the heatmap after inverse-variance weighting $w(t) = t^2$ (Section 4.3). The proof route passes through the endpoint residual $R_t := \|Y - \mu_p(X_t)\|_2$, whose \mathcal{L}^2 decomposition is recorded as the endpoint-space identity in Appendix A.5 by using Lemma 4.2. After that, Proposition 4.1 converts $\|Y - \mu_p(X_t)\|_2$ into the velocity residual $\|v_p(t, X_t) - (Y - X_0)\|_2$ used at inference. Theorem 4.3 is the implementation-aligned weighted velocity decomposition.

Lemma 4.2 (Tweedie). *Under Assumption A.1 in Appendix, fix $t \in (0, 1)$ and let $\mu_r(x) := \mathbb{E}_r[y \mid x_t = x]$ and $s_{r_t}(x) := \nabla \log r_t(x)$ for $r \in \{p, q\}$, where p, q denote the normal and abnormal image laws for y (with $x_t = (1 - t)x_0 + ty$ and $x_0 \sim \mathcal{N}(0, I)$ independent of y). The posterior mean satisfies $\mu_r(x) = \frac{1}{t}x + \frac{(1-t)^2}{t}s_{r_t}(x)$, and consequently*

$$\mu_q(x) - \mu_p(x) = \frac{(1-t)^2}{t}(s_{q_t}(x) - s_{p_t}(x)). \quad (6)$$

Proof. See Appendix A.3. □

Theorem 4.3 (Population decomposition of the weighted velocity mismatch). *Assume Assumption A.1. Fix $t \in (0, 1)$ and assume the path marginals p_t, q_t have smooth positive densities. Let*

$$v_p(t, x) := \mathbb{E}_p[Y - X_0 \mid X_t = x], \quad D_q(t) := \mathbb{E}_q\|Y - \mu_q(X_t)\|_2^2,$$

where $\mu_q(x) := \mathbb{E}_q[Y \mid X_t = x]$. If $J(q_t \| p_t) := \mathbb{E}_{X \sim q_t} [\|s_{q_t}(X) - s_{p_t}(X)\|_2^2] < \infty$, then

$$t^2 \mathbb{E}_q [\|v_p(t, X_t) - (Y - X_0)\|_2^2] = \underbrace{\frac{t^2}{(1-t)^2} D_q(t)}_{\text{weighted denoising error}} + \underbrace{(1-t)^2 J(q_t \| p_t)}_{\text{Fisher divergence}}. \quad (7)$$

Moreover, $\frac{t^2}{(1-t)^2} D_q(t) \leq d$ for residual dimension d , uniformly on $(0, 1)$, in particular the weighted denoising term stays bounded as $t \rightarrow 1$.

Proof. See Appendix A.6. □

Equation (7) shows how the velocity mismatch term works as an anomaly detection signal. Under normal data distribution $y \sim p$, the mismatch is governed only by a denoising error term (irreducible uncertainty). Under anomaly distribution $y \sim q$, the Fisher term appears, which quantifies discrepancy between the test-conditioned path marginal q_t and the normal marginal p_t . This Fisher term is the separation signal exploited by Flow Mismatching.

For localization, the same reasoning applies coordinate-wise. At each pixel, the squared oracle velocity mismatch $\|v_p(t, x) - (y - x_0)\|_2^2$ also decomposes into denoising error versus score mismatch as in Theorem 4.3. For RGB images, we average squared residuals over the three color channels, yielding a scalar anomaly score per pixel in the heatmap.

4.3 Time weighting: information-aware aggregation and endpoint stability

Along the affine path, the time t controls the effective noise level at which the model is queried.

We define the anomaly heatmap by aggregating velocity mismatches over time along the path, thereby obtaining a multi-scale score. Because each time t provide different amounts of information and estimator stability, time weighting is necessary to balance their contributions.

Different t corresponds to different noise levels, and variance scales differ across t . We therefore weight by inverse variance weighting in endpoint estimating error in y -space, yielding:

Proposition 4.4 (Time weight from inverse-variance weighting). *For the linear path $x_t = (1-t)x_0 + ty$ with $x_0 \sim \mathcal{N}(0, I)$, inverse-variance weighting of endpoint errors yields $w(t) = t^2$.*

Proof. See Appendix A.8 for details. □

Theorem 4.3 already packages this time weighting $w(t) = t^2$ to the corresponding population decomposition. Further, we have the following analysis.

Endpoint behavior. Equation (7) matches the time-weighted oracle analogue of the population score integrand in (5). It shows a time-dependent scale separation. As $t \rightarrow 0$, denoising term contributes $\sim t^2 \mathbb{E}_q[\|y - \mu_q(x_t)\|_2^2]$ while $(1-t)^2 J(q_t \| p_t)$ stays bounded if $J(q_t \| p_t)$ is bounded on $(0, 1)$. As $t \rightarrow 1$, $(1-t)^2 J(q_t \| p_t)$ vanishes and $\frac{t^2}{(1-t)^2} D_q(t)$ stays bounded in population because $D_q(t) = \mathbb{E}_q\|Y - \mu_q(X_t)\|_2^2$ contracts as $\mathcal{O}((1-t)^2/t^2)$, so $\frac{t^2}{(1-t)^2} D_q(t) \leq d$ uniformly even though unweighted residuals can blow up in variance. Appendix A.7 proves this contraction and explains excluding $t = 1$ numerically (velocity supervision still depends on unobserved X_0 once $x_t = y$). Thus early times emphasize Fisher (score) mismatch and late times emphasize denoising error under (7).

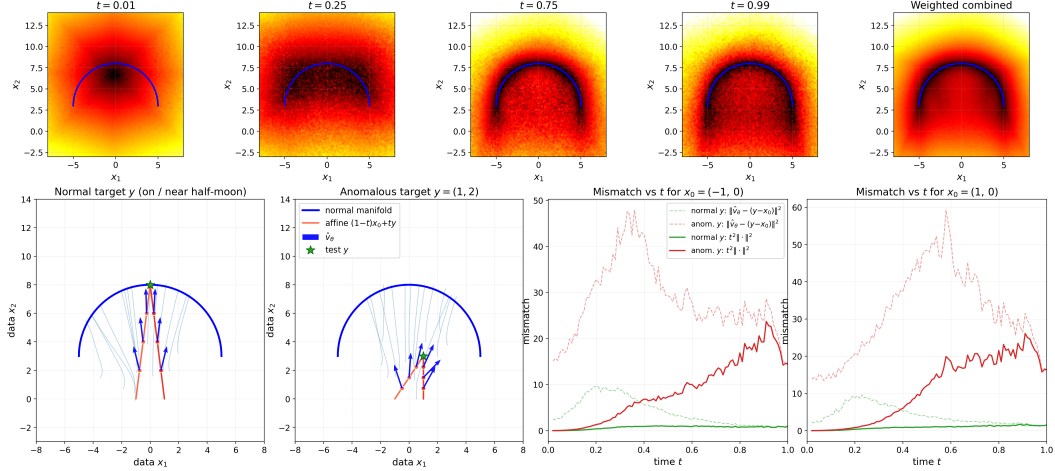


Figure 3: **Illustration of Flow Mismatching.** *Top:* normalized mismatch maps of $\|v_\theta(x_t, t) - (y - x_0)\|^2$ over (x_1, x_2) at several t and a t^2 -weighted aggregate (right); the blue arc is the normal support and scores grow off-manifold. Small t is smooth but weakly discriminative; large t tracks geometry better but is noisier; multi- t weighting combines both. *Bottom:* flows and affine paths for on-manifold y vs. off-manifold $y=(1, 2)$, with mismatch vs. t for $x_0 \in \{(-2, 0), (2, 0)\}$: the learned field stays aligned with the geometric velocity $y - x_0$ for normal targets (low green), but not for anomalies (high red). Dashed: raw squared residual; solid: t^2 -scaled.

Bias-variance trade-off across time. For the affine path $x_t = (1 - t)x_0 + ty$ with $x_0 \sim \mathcal{N}(0, I)$, the rescaled state $z_t := x_t/t = y + \frac{1-t}{t}x_0$ is a noisy observation of y with conditional variance $\text{Var}(z_t | y) = \frac{(1-t)^2}{t^2}I$. Thus small t has low signal-to-noise ratio, producing smooth but biased maps that poorly discriminate fine-scale perturbations, while large t gives sharper localization but higher finite- K Monte Carlo variance and more sensitivity to curvature near the data manifold. Aggregating over time with $w(t) = t^2$ therefore balances stable early semantic evidence with sharp late localization, reducing estimator variance while keeping the integral well posed near $t = 0$. Figure 3 summarizes the above analysis in one panel, and Appendix B.2 provides a dedicated toy visualization of per-time maps and the weighted combination.

4.4 Finite- K path aggregation and quantile bridge

We now connect finite- K path aggregation to the population signal in Theorem 4.3. The implementation samples K random source seeds and aggregates per-path mismatch at each pixel.

Path aggregation for localization. To approximate expectations over x_0 for a test image y , we sample K independent seeds $x_0^k \sim \mathcal{N}(0, I)$ and form per-pixel squared mismatches $Z_t^{(k)}(i) = \|v_\theta(x_t^k, t)(i) - (y - x_0^k)(i)\|_2^2$ with $x_t^k = (1 - t)x_0^k + ty$. We aggregate via $\delta_t(i) = \mathcal{A}(\{Z_t^{(k)}(i)\}_{k=1}^K)$; in particular $\delta_t^{\min}(i) = \min_{k \in [K]} Z_t^{(k)}(i)$ targets a lower tail over seeds (typical quantile order $\approx 1/K$). Corollary A.5 formalizes how independence across seeds turns single-path exceedance probabilities into exponential false-positive control under minimum aggregation.

Quantile bridge. Minimum (and lower-percentile) path aggregation targets lower tails of mismatch under random seeds X_0 for fixed y (Corollary A.5), complementing the expectation-level decomposition in Theorem 4.3. For the oracle marginal velocity field, fixing y and sampling only $X_0 \sim \mathcal{N}(0, I)$ gives an exact correspondence between conditional quantiles of the residual and of the score gap: for any $\alpha \in (0, 1)$,

$$Q_\alpha^{X_0}(\|v_p(t, X_t) - (y - X_0)\|_2 | y) = \frac{1-t}{t} Q_\alpha^{X_0}(\|s_{q_{t|y}}(X_t) - s_{p_t}(X_t)\|_2 | y). \quad (8)$$

Thus seed-wise quantiles track the score mismatch along the same test paths without a separate ‘‘quantile Tweedie’’ step; Appendix A.4 derives (8) from the fixed- y pathwise velocity–score identity.

At test time we observe v_θ rather than v_p . Let $G_t := \|s_{q_{t|y}}(X_t) - s_{p_t}(X_t)\|_2$ and $U_t := \frac{t}{1-t} \|v_\theta(X_t, t) - v_p(t, X_t)\|_2$. Then for $\alpha, \beta \in (0, 1)$ with $\alpha + \beta < 1$:

$$\mathbb{E}_Y \left[Q_{\alpha+\beta}^{X_0} \left(\|v_\theta(X_t, t) - (Y - X_0)\|_2^2 \mid Y \right) \right] \geq \frac{(1-t)^2}{t^2} \mathbb{E}_Y \left[\left(Q_\alpha^{X_0}(G_t \mid Y) - Q_{1-\beta}^{X_0}(U_t \mid Y) \right)_+^2 \right]. \quad (9)$$

Equation (9) is the learned-field analogue: it averages over $Y \sim q$ and separates an oracle score-gap quantile from an approximation tail via (α, β) after squaring (Appendix A.4). Thus the mean-level Theorem 4.3 captures expectations over (y, x_0) , while (8)–(9) formalize seed-wise robustness for a given test image. Finite-sample quantile arguments are in Appendix A.9.

Remark 4.5 (Average versus minimum path aggregation). The average aggregator $\delta_t^{\text{avg}}(i) = \frac{1}{K} \sum_{k=1}^K Z_t^{(k)}(i)$ targets the population mean in Theorem 4.3. In contrast, the minimum (or lower-percentile) aggregator targets robust lower-tail evidence across seeds, and is intentionally conservative: high anomaly scores persist only when the mismatch is consistently large across sampled paths. This conservative behavior is why our default uses minimum aggregation. While Theorem 4.3 explains the score-gap mechanism, the fixed- y quantile identity and minimum-aggregation corollary justify the robust path aggregation used in the heatmap.

Combining time aggregation (Section 4.3) with path aggregation yields our implemented heatmap $H(i) = \frac{1}{|\mathcal{T}|} \sum_{t \in \mathcal{T}} w(t) \delta_t(i)$, where $\delta_t(i) = \min_{k \in [K]} Z_t^{(k)}(i)$ uses the minimum aggregator, as justified in Remark 4.5. This directly implements the theoretical decomposition at the pixel level, and a conservative lower-tail analogue of the population mismatch signal.

5 Experiments

5.1 Setup

Datasets and metrics. **MVTec-AD** [Bergmann et al., 2019] contains 15 categories (5 objects, 10 textures) with 3,629 training and 1,725 test images. **VisA** [Zou et al., 2022] includes 12 SMD categories with 8,659 training and 2,162 test images. Training sets contain only normal images, while test sets include both normal and anomalous samples. All images are uniformly resized to 128×128 and normalized corresponding to normal images’ mean and standard deviation, without any other augmentation. AUROC, AP, and F1-max are reported for both image-level detection and pixel-level localization. AUPRO is also reported for localization, yielding 7 metrics in total.

Implementation details. We use U-Net with attention [Lipman et al., 2024] as the flow matching model. Our *default* setting is as follows. A single model with conditional category label is trained per dataset on normal images for 2,000 epochs, with StableAdamW optimizer, AMSGrad, a learning rate of $1e-4$, and batch size of 32. The basic channel dimension in U-Net is set to 64. See Appendix C for details. Experiments are conducted on 80GB NVIDIA A100. At inference, we sample $K = 10$ paths and use $T = 10$ time steps (i.e., $KT = 100$ model forward evaluations per image). The minimum aggregator over paths is applied.

5.2 Comparison with Reconstruction-based Methods

Flow Mismatching achieves competitive performances on MVTEC and VisA (Table 1), matching or surpassing SOTA reconstruction-based benchmarks including CFLOW-AD [Gudovskiy et al., 2022], RD4D [Deng and Li, 2022], UniAD [You et al., 2022], SimpleNet [Liu et al., 2023b], DeSTSeg [Zhang et al., 2023], HVQ-Trans [Lu et al., 2023], DiAD [He et al., 2024a], MambaAD [He et al., 2024b], ViTAD [Zhang et al., 2025b], AMDM Feng et al. [2025]. Efficiency comparison is in Table 3. Remarkably, our method demonstrates strong pixel-level localization performance, capable of capturing small anomalies accurately. See Figure 13, 14 in Appendix F for visualized results.

5.3 Comparison with Flow Matching-based Methods

Recent works have leveraged flow matching for anomaly detection. We implement and compare training-modified methods that apply different FM training objectives, including Reflect [Beizae et al., 2025], TCCM [Li et al., 2025b], and WT-Flow [Li et al., 2025a], and inference-only methods

Table 1: Comparison of reconstruction-based anomaly detection methods on MVTec-AD and VisA.

Method	MVTec-AD							VisA						
	Image-level			Pixel-level				Image-level			Pixel-level			
	AUROC	AP	F_1 -max	AUROC	AP	F_1 -max	PRO	AUROC	AP	F_1 -max	AUROC	AP	F_1 -max	PRO
RD4AD	94.6	96.5	95.2	96.1	48.6	53.8	91.1	92.4	92.4	89.6	98.1	38.0	42.6	91.8
CFLOW-AD	92.7	97.2	94.0	95.8	46.8	49.6	89.0	87.2	89.5	85.1	97.8	34.2	37.2	87.3
UniAD	96.5	98.8	96.2	96.8	43.4	49.5	90.7	88.8	90.8	85.8	98.3	33.7	39.0	85.5
SimpleNet	95.3	98.4	95.8	96.9	45.9	49.7	86.5	87.2	87.0	81.8	96.8	34.7	37.8	81.4
DeSTSeg	89.2	95.5	91.6	93.1	54.3	50.9	64.8	88.9	89.0	85.2	96.1	39.6	43.4	67.4
HVQ-Trans	98.0	99.5	97.5	97.3	48.2	53.3	91.4	93.2	92.8	87.6	98.7	35.0	39.6	86.3
DiAD	97.2	99.0	96.5	96.8	52.6	55.5	90.7	86.8	88.3	85.1	96.0	26.1	33.0	75.2
MambaAD	98.5	99.5	97.6	97.7	56.1	58.7	93.6	94.3	94.5	89.4	98.5	39.4	44.0	91.0
ViTAD	98.3	99.4	97.3	97.7	55.3	58.7	91.4	90.5	91.7	86.3	98.2	36.6	41.1	85.1
AMDM	98.4	99.0	97.4	97.5	51.5	56.1	92.6	94.8	95.6	91.1	98.8	39.8	43.5	88.4
Ours	98.7	99.5	97.7	97.7	67.5	64.8	91.9	98.0	98.4	95.2	97.5	40.2	45.8	90.6

Table 2: Comparison of flow matching based anomaly detection methods on MVTec-AD.

Method	Image-level			Pixel-level			
	AUROC	AP	F_1 -max	AUROC	AP	F_1 -max	PRO
Training-Modified FM							
Reflect	66.4	86.3	84.6	60.2	19.5	24.9	31.6
TCCM	53.6	77.7	85.1	73.0	23.1	28.8	49.9
WT-Flow	85.0	92.3	90.7	85.4	46.5	50.6	70.2
Inference-Only FM							
D-Flow	75.3	88.1	88.3	87.1	37.6	41.8	62.3
ReconFlow	91.8	97.2	94.3	92.4	53.8	56.1	72.7
Ours	98.7	99.5	97.7	97.7	67.5	64.8	91.9

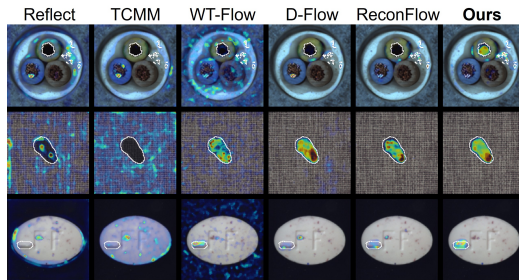


Figure 4: Visualization of FM-based heatmaps. Ground truths are shown by white lines.

that rely on test-time detection, including D-Flow [Ben-Hamu et al., 2024] accelerated by Flow-Grad Liu et al. [2023a], and ReconFlow, a reconstruction-style counterpart of our method. For controlled comparison, we adapt all FM baselines to the same image-domain U-Net backbone and identical training/inference protocol. Therefore these numbers should be interpreted as same-backbone controlled comparisons rather than reproductions of each method’s best feature-domain setting; see Appendix C for implementation details. Overall, Flow Mismatching yields the leading best results. See visualization results in Figure 4 and detailed per-class comparison in Appendix E.

5.4 Ablation Study

Test-time compute trade-offs. We analyze how the number of paths K and time steps T affects model performance and throughput on MVTec. Detailed results are listed in Table 6, and the trade-off curves are shown in Figure 2. Larger K, T improves performance monotonically, and even the smallest setting we consider ($K=T=2$, FPS=86.4) surpasses a few reconstruction based SOTAs and all the flow matching based methods, yielding reasonable and acceptable results. The qualitative mechanism behind this trend is consistent with the controlled toy visualization in Appendix B.1.

Path aggregator. By default, we aggregate the K paths using the minimum aggregator, which is effective in practice and consistent with the quantile-based analysis in Section 4: minimum aggregation suppresses path specific spurious responses and reduces false positives. We also compare alternative aggregators, including the average and the 10th, 20th, and 30th percentiles, in Table 7.

Condition label vs. pooled categories. In the default setting we applied a single flow matching model with conditional category label to handle all the categories. We also trained an unconditional model, and figured out the method also works for pooled categories case. Under this setting, our method still achieves the best pixel-level AP/ F_1 -max on both datasets, as well as the best image-level AUROC/AP/ F_1 -max on VisA, and surpasses a few SOTAs. Detailed per-class comparison is in Table 8 in Appendix E. A toy example reasoning for the pooled category setting is in Appendix B.

6 References

- Abdelrahman Alzarooni, Ehtesham Iqbal, Samee Ullah Khan, Sajid Javed, Brain Moyo, and Yusra Abdulrahman. Anomaly detection for industrial applications, its challenges, solutions, and future directions: A review. *arXiv preprint arXiv:2501.11310*, 2025.
- Farzad Beizae et al. Reflect: Rectified flows for efficient brain anomaly correction transport. In *Medical Image Computing and Computer Assisted Intervention (MICCAI)*, 2025.
- Heli Ben-Hamu, Omri Puny, Itai Gat, Brian Karrer, Uriel Singer, and Yaron Lipman. D-flow: differentiating through flows for controlled generation. In *Proceedings of the 41st International Conference on Machine Learning*, pages 3462–3483, 2024.
- Paul Bergmann, Michael Fauser, David Sattlegger, and Carsten Steger. Mvtec ad—a comprehensive real-world dataset for unsupervised anomaly detection. In *2019 IEEE/CVF Conference on Computer Vision and Pattern Recognition (CVPR)*, pages 9584–9592. IEEE Computer Society, 2019.
- Mathilde Caron, Hugo Touvron, Ishan Misra, Hervé Jégou, Julien Mairal, Piotr Bojanowski, and Armand Joulin. Emerging properties in self-supervised vision transformers. In *Proceedings of the IEEE/CVF international conference on computer vision*, pages 9650–9660, 2021.
- Hanqiu Deng and Xingyu Li. Anomaly detection via reverse distillation from one-class embedding. In *2022 IEEE/CVF Conference on Computer Vision and Pattern Recognition (CVPR)*, pages 9727–9736. IEEE, 2022.
- Alexey Dosovitskiy, Lucas Beyer, Alexander Kolesnikov, Dirk Weissenborn, Xiaohua Zhai, Thomas Unterthiner, Mostafa Dehghani, Matthias Minderer, Georg Heigold, Sylvain Gelly, et al. An image is worth 16x16 words: Transformers for image recognition at scale. In *International Conference on Learning Representations*, 2021.
- Yaoyuan Feng, Wenchao Chen, Yuxin Li, Bo Chen, Yubiao Wang, Zixuan Zhao, Hongwei Liu, and Mingyuan Zhou. Omiad: One-step adaptive masked diffusion model for multi-class anomaly detection via adversarial distillation. In *Forty-second International Conference on Machine Learning*, pages 16604–16633, 2025.
- Matic Fučka, Vitjan Zavrtanik, and Danijel Skočaj. Transfusion—a transparency-based diffusion model for anomaly detection. In *European conference on computer vision*, pages 91–108. Springer, 2024.
- Albert Gu and Tri Dao. Mamba: Linear-time sequence modeling with selective state spaces. *arXiv preprint arXiv:2312.00752*, 2023.
- Denis Gudovskiy, Shun Ishizaka, and Kazuki Kozuka. Cflow-ad: Real-time unsupervised anomaly detection with localization via conditional normalizing flows. In *Proceedings of the IEEE/CVF winter conference on applications of computer vision*, pages 98–107, 2022.
- Jia Guo, Shuai Lu, Weihang Zhang, Fang Chen, Huiqi Li, and Hongen Liao. Dinomaly: The less is more philosophy in multi-class unsupervised anomaly detection. In *Proceedings of the Computer Vision and Pattern Recognition Conference*, pages 20405–20415, 2025.
- Haoyang He, Jiangning Zhang, Hongxu Chen, Xuhai Chen, Zhishan Li, Xu Chen, Yabiao Wang, Chengjie Wang, and Lei Xie. A diffusion-based framework for multi-class anomaly detection. In *Proceedings of the AAAI conference on artificial intelligence*, volume 38, pages 8472–8480, 2024a.
- Haoyang He et al. Mambaad: Exploring state space models for multi-class unsupervised anomaly detection. In *Advances in Neural Information Processing Systems (NeurIPS)*, 2024b.
- Yangfan He, Xinyan Wang, and Tianyu Shi. Ddpm-moco: Advancing industrial surface defect generation and detection with generative and contrastive learning. In *International Joint Conference on Artificial Intelligence*, pages 34–49. Springer, 2024c.
- Andrej Leban. Energy-tweedie: Score meets score, energy meets energy. *arXiv preprint arXiv:2512.23818*, 2025.

- Liangwei Li, Lin Liu, Juanxiu Liu, Jing Zhang, Ruqian Hao, and Xiaohui Du. How and why: Taming flow matching for unsupervised anomaly detection and localization. In *arXiv preprint arXiv:2508.05461*, 2025a.
- Zhong Li et al. Scalable, explainable and provably robust anomaly detection with one-step flow matching. In *Advances in Neural Information Processing Systems (NeurIPS)*, 2025b.
- Yaron Lipman, Ricky T. Q. Chen, Heli Ben-Hamu, Maximilian Nickel, and Matt Le. Flow matching for generative modeling. *arXiv preprint arXiv:2210.02747*, 2023.
- Yaron Lipman, Marton Havasi, Peter Holderrieth, Neta Shaul, Matt Le, Brian Karrer, Ricky T. Q. Chen, David Lopez-Paz, Heli Ben-Hamu, and Itai Gat. Flow matching guide and code, 2024. URL <https://arxiv.org/abs/2412.06264>.
- Xingchao Liu, Lemeng Wu, Shujian Zhang, Chengyue Gong, Wei Ping, and Qiang Liu. Flowgrad: Controlling the output of generative odes with gradients. In *Proceedings of the IEEE/CVF Conference on Computer Vision and Pattern Recognition*, pages 24335–24344, 2023a.
- Zhikang Liu, Yiming Zhou, Yuansheng Xu, and Zilei Wang. Simplenet: A simple network for image anomaly detection and localization. In *Proceedings of the IEEE/CVF Conference on Computer Vision and Pattern Recognition*, pages 20402–20411, 2023b.
- Ruiying Lu, YuJie Wu, Long Tian, Dongsheng Wang, Bo Chen, Xiyang Liu, and Ruimin Hu. Hierarchical vector quantized transformer for multi-class unsupervised anomaly detection. In *Proceedings of the 37th International Conference on Neural Information Processing Systems*, pages 8487–8500, 2023.
- Francesco Vaselli et al. It’s not a fad: first results in using flows for unsupervised anomaly detection at 40 mhz at the large hadron collider. *arXiv preprint arXiv:2508.11594*, 2025.
- Yue Wang, Yong Yang, Mingsheng Liu, Xianghong Tang, Haibin Wang, Zhifeng Hao, Ze Shi, Gang Wang, Botao Jiang, and Chunyang Liu. Industrial product surface defect detection via the fast denoising diffusion implicit model. *International Journal of Machine Learning and Cybernetics*, 15(11):5091–5106, 2024.
- Zekang Weng, Jinjin Shi, Jinwei Wang, and Zeming Han. Hdm: Hybrid diffusion model for unified image anomaly detection. *arXiv preprint arXiv:2502.19200*, 2025.
- Ruyi Xu, Yen-Tzu Chiu, Tai-I Chen, Oscar Chew, Yung-Yu Chuang, and Wen-Huang Cheng. Training-free industrial defect generation with diffusion models. In *Proceedings of the IEEE/CVF International Conference on Computer Vision*, pages 24214–24223, 2025.
- Zhiyuan You, Lei Cui, Yujun Shen, Kai Yang, Xin Lu, Yu Zheng, and Xinyi Le. A unified model for multi-class anomaly detection. *Advances in Neural Information Processing Systems*, 35: 4571–4584, 2022.
- Hui Zhang, Zheng Wang, Dan Zeng, Zuxuan Wu, and Yu-Gang Jiang. Diffusionad: Norm-guided one-step denoising diffusion for anomaly detection. *IEEE Transactions on Pattern Analysis and Machine Intelligence*, 2025a.
- Jiangning Zhang, Xuhai Chen, Yabiao Wang, Chengjie Wang, Yong Liu, Xiangtai Li, Ming-Hsuan Yang, and Dacheng Tao. Exploring plain vit reconstruction for multi-class unsupervised anomaly detection. *CVIU*, 2025b.
- Xuan Zhang, Shiyu Li, Xi Li, Ping Huang, Jiulong Shan, and Ting Chen. Destseg: Segmentation guided denoising student-teacher for anomaly detection. In *2023 IEEE/CVF Conference on Computer Vision and Pattern Recognition (CVPR)*, pages 3914–3923. IEEE, 2023.
- Zhengyu Zhou and Weiwei Liu. An error analysis of flow matching for deep generative modeling. In *Forty-second International Conference on Machine Learning*, pages 78903–78932, 2025.
- Yang Zou, Jongheon Jeong, Latha Pemula, Dongqing Zhang, and Onkar Dabeer. Spot-the-difference self-supervised pre-training for anomaly detection and segmentation. In *European Conference on Computer Vision*, pages 392–408, 2022.

A Proofs and Additional Theorems

In this appendix, we provide detailed derivations.

A.1 Test-time Linear Interpolation Assumption

Assumption A.1 (Linear interpolation for test-time analysis). Fix $t \in (0, 1)$. Let $y \in \mathbb{R}^d$ be the (possibly anomalous) data variable, distributed according to a law $r \in \{p, q\}$. Let $x_0 \sim \mathcal{N}(0, I_d)$ be independent of y . Define the test-time linear interpolation path $x_t = (1-t)x_0 + ty$. Then conditional on y , x_t is Gaussian: $x_t | y \sim \mathcal{N}(ty, (1-t)^2 I_d)$.

A.2 Proof of Proposition 4.1

Proof. Fix $t \in (0, 1)$ and define the affine path

$$x_t = (1-t)x_0 + ty.$$

First note the deterministic identity

$$y - x_t = y - (1-t)x_0 - ty = (1-t)(y - x_0). \quad (\text{A.0})$$

Now define

$$\mu_p(x) := \mathbb{E}_p[y | x_t = x], \quad v_p(t, x) := \mathbb{E}_p[y - x_0 | x_t = x].$$

Using (A.0), we can rewrite y pointwise as

$$y = x_t + (1-t)(y - x_0).$$

Taking conditional expectation given $x_t = x$ (under the normal law p) yields

$$\mu_p(x) = \mathbb{E}_p[y | x_t = x] = \mathbb{E}_p[x_t + (1-t)(y - x_0) | x_t = x] = x + (1-t) \mathbb{E}_p[y - x_0 | x_t = x] = x + (1-t)v_p(t, x).$$

Substituting $x = x_t$ and using (A.0) again gives

$$y - \mu_p(x_t) = y - x_t - (1-t)v_p(t, x_t) = (1-t)(y - x_0) - (1-t)v_p(t, x_t) = (1-t) \left((y - x_0) - v_p(t, x_t) \right),$$

which proves the first identity. Taking squared norms yields

$$\|y - \mu_p(x_t)\|^2 = (1-t)^2 \|v_p(t, x_t) - (y - x_0)\|^2.$$

□

A.3 Proof of Lemma 4.2

Proof. Fix $t \in (0, 1)$ and write the path as

$$x_t = (1-t)x_0 + ty = ty + \sigma\varepsilon, \quad \varepsilon \sim \mathcal{N}(0, I_d), \quad \sigma := 1-t,$$

so that conditional on y we have $x_t | y \sim \mathcal{N}(ty, \sigma^2 I_d)$. Let $\varphi_\sigma(u)$ denote the $\mathcal{N}(0, \sigma^2 I_d)$ density.

For any law r on y , the marginal density of x_t is the Gaussian convolution

$$r_t(x) = \int_{\mathbb{R}^d} r(y) \varphi_\sigma(x - ty) dy.$$

Differentiate under the integral sign (justified since φ_σ is smooth and integrable):

$$\nabla_x r_t(x) = \int r(y) \nabla_x \varphi_\sigma(x - ty) dy = -\frac{1}{\sigma^2} \int (x - ty) r(y) \varphi_\sigma(x - ty) dy.$$

Rearranging gives

$$\sigma^2 \nabla_x r_t(x) = -x r_t(x) + t \int y r(y) \varphi_\sigma(x - ty) dy.$$

Divide both sides by $t r_t(x)$ to obtain

$$\frac{1}{r_t(x)} \int y r(y) \varphi_\sigma(x - ty) dy = \frac{1}{t} x + \frac{\sigma^2}{t} \frac{\nabla_x r_t(x)}{r_t(x)} = \frac{1}{t} x + \frac{\sigma^2}{t} \nabla_x \log r_t(x).$$

The left-hand side is exactly $\mathbb{E}_r[y \mid x_t = x]$ by Bayes' rule, hence

$$\mathbb{E}_r[y \mid x_t = x] = \frac{1}{t}x + \frac{(1-t)^2}{t} s_{r_t}(x),$$

where $s_{r_t} = \nabla \log r_t$ is the score of the marginal. The ‘‘consequently’’ statement follows by subtracting the cases $r = q$ and $r = p$.

Part (ii). Fix y and $t \in (0, 1)$, and write $X_t = (1-t)x_0 + ty$ with $x_0 \sim \mathcal{N}(0, I)$. Conditional on y , $X_t \sim q_{t|y} = \mathcal{N}(ty, (1-t)^2 I)$. The same convolution calculation as in part (i), applied to a Dirac law on y convolved with Gaussian noise, yields

$$y = \frac{1}{t}X_t + \frac{(1-t)^2}{t} s_{q_{t|y}}(X_t).$$

Also, part (i) applied to the marginal p_t gives

$$\mu_p(X_t) = \mathbb{E}_p[y \mid X_t] = \frac{1}{t}X_t + \frac{(1-t)^2}{t} s_{p_t}(X_t).$$

Subtracting yields

$$y - \mu_p(X_t) = \frac{(1-t)^2}{t} (s_{q_{t|y}}(X_t) - s_{p_t}(X_t)).$$

Taking Euclidean norms and using Proposition 4.1 in the form $\|y - \mu_p(X_t)\| = (1-t)\|v_p(t, X_t) - (y - X_0)\|$ yields the pathwise velocity–score identity (conditional on y)

$$(1-t)\|v_p(t, X_t) - (y - X_0)\|_2 = \frac{(1-t)^2}{t} \|s_{q_{t|y}}(X_t) - s_{p_t}(X_t)\|_2. \quad (10)$$

□

A.4 Learned flows: pointwise control

Lemma 4.2(ii) establishes (10). Dividing (10) by the scalar $1-t > 0$ gives $\|v_p(t, X_t) - (y - X_0)\|_2 = \frac{1-t}{t} \|s_{q_{t|y}}(X_t) - s_{p_t}(X_t)\|_2$, so scaling by $\frac{1-t}{t} > 0$ preserves conditional quantiles in X_0 and yields (8) from Section 4.4.

For fixed y and $t \in (0, 1)$, let

$$\begin{aligned} \tilde{L}_t^\theta(y) &:= \|v_\theta(X_t, t) - (y - X_0)\|_2, & \tilde{E}_t^\theta(y) &:= \|v_\theta(X_t, t) - v_p(t, X_t)\|_2, \\ G_t(y) &:= \|s_{q_{t|y}}(X_t) - s_{p_t}(X_t)\|_2, \end{aligned}$$

where $X_t = (1-t)X_0 + ty$ and $X_0 \sim \mathcal{N}(0, I)$.

Proposition A.2 (Learned-field quantile lower bound). *For any $\alpha, \beta \in (0, 1)$ with $\alpha + \beta < 1$,*

$$Q_{\alpha+\beta}^{X_0}(\tilde{L}_t^\theta(y) \mid y) \geq \left[\frac{1-t}{t} Q_\alpha^{X_0}(G_t(y) \mid y) - Q_{1-\beta}^{X_0}(\tilde{E}_t^\theta(y) \mid y) \right]_+. \quad (11)$$

Consequently,

$$Q_{\alpha+\beta}^{X_0}((\tilde{L}_t^\theta(y))^2 \mid y) \geq \left[\frac{1-t}{t} Q_\alpha^{X_0}(G_t(y) \mid y) - Q_{1-\beta}^{X_0}(\tilde{E}_t^\theta(y) \mid y) \right]_+^2. \quad (12)$$

Proof. By triangle inequality,

$$\tilde{L}_t^\theta(y) \geq \|v_p(t, X_t) - (y - X_0)\|_2 - \tilde{E}_t^\theta(y).$$

Using (10) after dividing by $1-t$,

$$\|v_p(t, X_t) - (y - X_0)\|_2 = \frac{1-t}{t} G_t(y).$$

Hence pointwise

$$\tilde{L}_t^\theta(y) \geq \frac{1-t}{t} G_t(y) - \tilde{E}_t^\theta(y).$$

Applying the standard one-sided quantile inequality $Q_{\alpha+\beta}(A - B) \geq Q_\alpha(A) - Q_{1-\beta}(B)$ and then clipping at zero gives (11). Since $x \mapsto x^2$ is monotone on $[0, \infty)$ and $\tilde{L}_t^\theta(y) \geq 0$, (12) follows. □

Taking expectation over Y , rewrite (12) using $Q_{1-\beta}^{X_0}(\tilde{E}_t^\theta(Y) | Y) = \frac{1-t}{t} Q_{1-\beta}^{X_0}(U_t | Y)$ for $U_t = \frac{t}{1-t} \tilde{E}_t^\theta(Y)$ (matching the main-text definition of U_t):

$$Q_{\alpha+\beta}^{X_0}\left((\tilde{E}_t^\theta(Y))^2 | Y\right) \geq \frac{(1-t)^2}{t^2} \left[Q_{\alpha}^{X_0}(G_t(Y) | Y) - Q_{1-\beta}^{X_0}(U_t | Y) \right]_+^2,$$

which yields the main-text quantile bridge (9).

A.5 Endpoint-space decomposition

Proposition A.3 (Endpoint \mathcal{L}^2 decomposition). *Assume Assumption A.1. Fix $t \in (0, 1)$ and suppose the path marginals p_t, q_t admit smooth positive densities. Let $(X_0, Y) \sim q$ denote independent $X_0 \sim \mathcal{N}(0, I)$ and anomaly image Y , and set $X_t := (1-t)X_0 + tY$. Define $\mu_r(x) := \mathbb{E}_r[Y | X_t = x]$ for $r \in \{p, q\}$ and assume $J(q_t \| p_t) < \infty$. Then*

$$\mathbb{E}_q \|Y - \mu_p(X_t)\|_2^2 = \mathbb{E}_q \|Y - \mu_q(X_t)\|_2^2 + \frac{(1-t)^4}{t^2} J(q_t \| p_t). \quad (13)$$

Proof. Fix $t \in (0, 1)$ and work under the anomaly law q for (X_0, Y) . Let

$$\mu_r(x) := \mathbb{E}_r[Y | X_t = x], \quad r \in \{p, q\}.$$

Define the q -residual and the mean-shift term

$$e := Y - \mu_q(X_t), \quad \delta := \mu_q(X_t) - \mu_p(X_t).$$

Then $Y - \mu_p(X_t) = e + \delta$. Expanding the squared norm gives

$$\|Y - \mu_p(X_t)\|_2^2 = \|e\|_2^2 + \|\delta\|_2^2 + 2\langle e, \delta \rangle.$$

Taking expectation under q yields

$$\mathbb{E}_q \|Y - \mu_p(X_t)\|_2^2 = \mathbb{E}_q \|e\|_2^2 + \mathbb{E}_q \|\delta\|_2^2 + 2\mathbb{E}_q \langle e, \delta \rangle.$$

The cross term vanishes by orthogonality of conditional expectation: δ is measurable with respect to X_t , while

$$\mathbb{E}_q [e | X_t] = \mathbb{E}_q [Y - \mu_q(X_t) | X_t] = 0.$$

Hence

$$\mathbb{E}_q \|Y - \mu_p(X_t)\|_2^2 = \mathbb{E}_q \|Y - \mu_q(X_t)\|_2^2 + \mathbb{E}_q \|\mu_q(X_t) - \mu_p(X_t)\|_2^2.$$

Applying Lemma 4.2 (Tweedie),

$$\mu_q(x) - \mu_p(x) = \frac{(1-t)^2}{t} (s_{q_t}(x) - s_{p_t}(x)),$$

so

$$\mathbb{E}_q \|\mu_q(X_t) - \mu_p(X_t)\|_2^2 = \left(\frac{(1-t)^2}{t} \right)^2 J(q_t \| p_t),$$

which is (13). □

A.6 Proof of Theorem 4.3

Proof. Let $R_t := \|Y - \mu_p(X_t)\|_2$. By Proposition 4.1,

$$t^2 \mathbb{E}_q \|v_p(t, X_t) - (Y - X_0)\|_2^2 = \frac{t^2}{(1-t)^2} \mathbb{E}_q [R_t^2].$$

Proposition A.3 (Appendix A.5) gives the \mathcal{L}^2 decomposition of $\mathbb{E}_q [R_t^2]$ in Equation (13); substituting yields (7).

For the boundedness claim, let

$$Z_t := X_t/t = Y + \frac{1-t}{t} X_0.$$

Since $\mu_q(X_t) = \mathbb{E}_q [Y | X_t]$ is the minimum-MSE estimator of Y from X_t ,

$$D_q(t) \leq \mathbb{E}_q \|Y - Z_t\|_2^2 = d \frac{(1-t)^2}{t^2}.$$

Multiplying by $t^2/(1-t)^2$ gives $\frac{t^2}{(1-t)^2} D_q(t) \leq d$. □

A.7 Late-time behavior: contraction versus algebraic prefactors

Theorem 4.3 rewrites $t^2 \mathbb{E}_q \|v_p(t, X_t) - (Y - X_0)\|_2^2$ as in (7), with $D_q(t) = \mathbb{E}_q \|Y - \mu_q(X_t)\|_2^2$ and $\mu_q(x) = \mathbb{E}_q[Y \mid X_t = x]$ the Bayes estimator of Y under q from the noisy affine statistic $X_t = (1-t)X_0 + tY$. Read naïvely from the velocity parametrization, the coefficient $\frac{t^2}{(1-t)^2}$ diverges as $t \rightarrow 1$, which can suggest catastrophic endpoint scaling. This is misleading for the weighted population mismatch in (7).

Posterior contraction cancels the prefactor. The term $D_q(t)$ is mean squared error (Bayes risk) under law q , hence bounded above by the risk of any measurable estimator of Y from X_t . Define $Z_t := X_t/t = Y + \frac{1-t}{t}X_0$. Conditional on Y , Z_t is an unbiased estimator of Y with isotropic error variance $\frac{(1-t)^2}{t^2}I_d$, so

$$\mathbb{E}_q \|Y - Z_t\|_2^2 = \mathbb{E}_q [\mathbb{E}_q [\|Y - Z_t\|_2^2 \mid Y]] = d \frac{(1-t)^2}{t^2}.$$

Since $\mu_q(X_t)$ attains the minimum mean squared error among estimators of Y from X_t under q ,

$$D_q(t) \leq \mathbb{E}_q \|Y - Z_t\|_2^2 = d \frac{(1-t)^2}{t^2},$$

and therefore

$$\frac{t^2}{(1-t)^2} D_q(t) \leq d.$$

Thus the dangerous-looking prefactor is exactly compensated by posterior contraction of $\mu_q(X_t)$ toward Y as $t \rightarrow 1$; the weighted denoising contribution is dimension-wise $\mathcal{O}(1)$ uniformly on $(0, 1)$.

Why $t = 1$ is still excluded in practice. Population boundedness as $t \uparrow 1$ concerns expectations under the transport path and does not remove numerical degeneracy at the literal endpoint. At $t = 1$ one has $X_t = Y$ almost surely, so conditioning on X_t yields a singular posterior for (Y, X_0) given only Y . Moreover, along $t < 1$ the affine-path velocity target depends on the pair (Y, X_0) through $Y - X_0$, while at $t = 1$ the state $X_t = Y$ no longer identifies X_0 ; score identities also exhibit $(1-t)^{-1}$ scaling. Accordingly, implementations discretize $\mathcal{T} \subset (0, 1)$ as in Section 3.

A.8 Proof of Proposition 4.4

Proof. Along the linear path $x_t = (1-t)x_0 + ty$, define the rescaled observation

$$z_t := \frac{x_t}{t} = y + \frac{1-t}{t}x_0,$$

so that conditional on y , $z_t \mid y \sim \mathcal{N}(y, \sigma_t^2 I)$ with

$$\sigma_t^2 = \left(\frac{1-t}{t}\right)^2.$$

Thus the noise level depends on t and a standard inverse-variance (GLS) weight in y -space is

$$w_y(t) \propto \frac{1}{\sigma_t^2} = \frac{t^2}{(1-t)^2}.$$

Now define the velocity residual

$$r_\theta(x_0, y, t) := v_\theta(x_t, t) - (y - x_0).$$

If we form the induced endpoint/denoiser estimate

$$\hat{y}_\theta(x_t, t) := x_t + (1-t)v_\theta(x_t, t),$$

then using the deterministic identity $y - x_t = (1-t)(y - x_0)$ we obtain

$$\hat{y}_\theta - y = x_t + (1-t)v_\theta(x_t, t) - y = -(1-t)(v_\theta(x_t, t) - (y - x_0)) = -(1-t)r_\theta(x_0, y, t),$$

hence

$$\|\hat{y}_\theta - y\|^2 = (1-t)^2 \|r_\theta(x_0, y, t)\|^2.$$

Therefore inverse-variance weighting of squared endpoint errors gives

$$w_y(t) \|\hat{y}_\theta - y\|^2 \propto \frac{t^2}{(1-t)^2} (1-t)^2 \|r_\theta\|^2 = t^2 \|r_\theta\|^2,$$

so the induced weight on squared velocity residuals is $w(t) = t^2$ (up to an irrelevant constant). \square

A.9 Statistical Guarantees for Monte Carlo Estimators

This section provides formal concentration bounds for the Monte Carlo path averaging estimator. These results justify the finite- K approximation of the population score and explain why minimum aggregation reduces false positives.

A.9.1 What we are estimating

For a test image y , time $t \in \mathcal{T}$, and pixel $p \in \Omega$, define

$$Z_t^{(k)}(p) := \|v_\theta(x_t^{(k)}, t)(p) - (y - x_0^{(k)})(p)\|_2^2,$$

where $x_0^{(k)} \sim \mathcal{N}(0, I)$ are i.i.d. Gaussian seeds and $x_t^{(k)} = (1-t)x_0^{(k)} + ty$. The population target is $m_{t,p} := \mathbb{E}_{x_0} [Z_t(p)]$, which corresponds to the expected squared velocity mismatch at pixel p and time t . The Monte Carlo average estimator is

$$\hat{m}_{t,p} := \frac{1}{K} \sum_{k=1}^K Z_t^{(k)}(p) = \delta_t^{\text{avg}}(p).$$

This connects directly to the population score and Theorem 4.3.

A.9.2 Concentration of the path average

Lemma A.4 (Concentration of path averaging). *Fix $(t, p) \in \mathcal{T} \times \Omega$. Let $Z_t^{(1)}(p), \dots, Z_t^{(K)}(p)$ be i.i.d. with mean $m_{t,p}$. Assume $Z_t(p) - m_{t,p}$ is sub-exponential with $\|Z_t(p) - m_{t,p}\|_{\psi_1} \leq \nu_{t,p}$. Then for all $\varepsilon > 0$,*

$$\Pr(|\hat{m}_{t,p} - m_{t,p}| \geq \varepsilon) \leq 2 \exp \left[-cK \min \left(\frac{\varepsilon^2}{\nu_{t,p}^2}, \frac{\varepsilon}{\nu_{t,p}} \right) \right],$$

where $c > 0$ is a universal constant.

Proof. Let $X_k := Z_t^{(k)}(p) - m_{t,p}$, so $\mathbb{E}[X_k] = 0$ and $\|X_k\|_{\psi_1} \leq \nu_{t,p}$. By the Bernstein inequality for sums of independent sub-exponential variables

$$\Pr \left(\left| \frac{1}{K} \sum_{k=1}^K X_k \right| \geq \varepsilon \right) \leq 2 \exp \left[-cK \min \left(\frac{\varepsilon^2}{\nu_{t,p}^2}, \frac{\varepsilon}{\nu_{t,p}} \right) \right].$$

Since $\frac{1}{K} \sum_{k=1}^K X_k = \hat{m}_{t,p} - m_{t,p}$, the claim follows. \square

The sub-exponential assumption is reasonable in our setting: $Z_t(p)$ is a squared norm of a quantity that is roughly sub-Gaussian when the randomness comes from Gaussian x_0 and the network output v_θ is Lipschitz/bounded. The fact that “squared sub-Gaussian is sub-exponential” is standard in high-dimensional probability.

A.9.3 Minimum aggregation suppresses false positives

Corollary A.5 (Minimum aggregation suppresses false positives). *Fix $(t, p) \in \mathcal{T} \times \Omega$ and let $\delta_t^{\min}(p) := \min_{k \in [K]} Z_t^{(k)}(p)$. Then for any threshold τ ,*

$$\Pr(\delta_t^{\min}(p) > \tau) = \Pr(Z_t(p) > \tau)^K.$$

Proof. Because $Z_t^{(k)}(p)$ are i.i.d.,

$$\Pr(\delta_t^{\min}(p) > \tau) = \Pr(\forall k, Z_t^{(k)}(p) > \tau) = \prod_{k=1}^K \Pr(Z_t(p) > \tau) = \Pr(Z_t(p) > \tau)^K.$$

\square

Thus if a spurious pixel exceeds τ with probability r for a single seed, minimum aggregation reduces it to r^K . This exponential suppression directly supports our design choice of using minimum aggregation for robustness to spurious detections.

A.9.4 Uniform control over all pixels and times

Corollary A.6 (Uniform control over all pixels and times). *Assume Lemma A.4 holds with a common bound $\|Z_t(p) - m_{t,p}\|_{\psi_1} \leq \nu$ for all $(t, p) \in \mathcal{T} \times \Omega$. Let $M := |\mathcal{T}||\Omega|$. Then with probability at least $1 - \delta$,*

$$\max_{t \in \mathcal{T}} \max_{p \in \Omega} |\hat{m}_{t,p} - m_{t,p}| \leq C\nu \max\left(\sqrt{\frac{\log(2M/\delta)}{K}}, \frac{\log(2M/\delta)}{K}\right),$$

for a universal constant $C > 0$.

Proof. Apply Lemma A.4 to each (t, p) with failure probability δ/M :

$$\Pr(|\hat{m}_{t,p} - m_{t,p}| \geq \varepsilon) \leq \frac{\delta}{M},$$

where choosing $\varepsilon = C\nu \max\left(\sqrt{\frac{\log(2M/\delta)}{K}}, \frac{\log(2M/\delta)}{K}\right)$ makes the RHS at most δ/M by the lemma's exponential tail. Taking a union bound over all M pairs (t, p) yields the claim. \square

This shows that we only need $K \gtrsim \log(|\Omega||\mathcal{T}|)$ paths to get uniform control over all pixels and times. This is the standard “log dimension” effect in high-dimensional statistics: the sample complexity scales logarithmically with the ambient dimension, making the method practical even for high-resolution images.

B Toy examples and Analysis

B.1 Toy example 1: visualization of how increasing test-time compute affects anomaly scores

To illustrate the behavior of flow mismatching in a geometry-constrained setting, we use a 2D half-moon toy example. The normal data distribution is supported on the upper semicircle with center $c = (0, 3)$ and radius $r = 5$, i.e., $\{(x_1, x_2) : (x_1 - c_1)^2 + (x_2 - c_2)^2 = r^2, x_2 \geq c_2\}$. The source distribution is a two-dimensional standard Gaussian. We evaluate scores on a rectangular grid $x_1 \in [-8, 8]$, $x_2 \in [-3, 14]$, train a time-conditioned MLP flow-matching model, and compute anomaly scores for each grid point p . Path-wise residuals are aggregated using the minimum across Gaussian draws (Eq. 3), then aggregated over time using Eq. 4 with $w(t) = t^2$.

Figure 5 focuses on sensitivity to (T, K) in the half-moon setting. Across panels, anomaly scores remain low near the normal manifold and increase away from it, showing that the recovered score geometry is consistent with the underlying support. Increasing temporal resolution T reduces discretization noise and yields smoother maps. Increasing the number of Gaussian draws K stabilizes the path aggregation and, under the minimum operator in Eq. 3, produces a more conservative estimate with broader low-score regions near normal-support geometry.

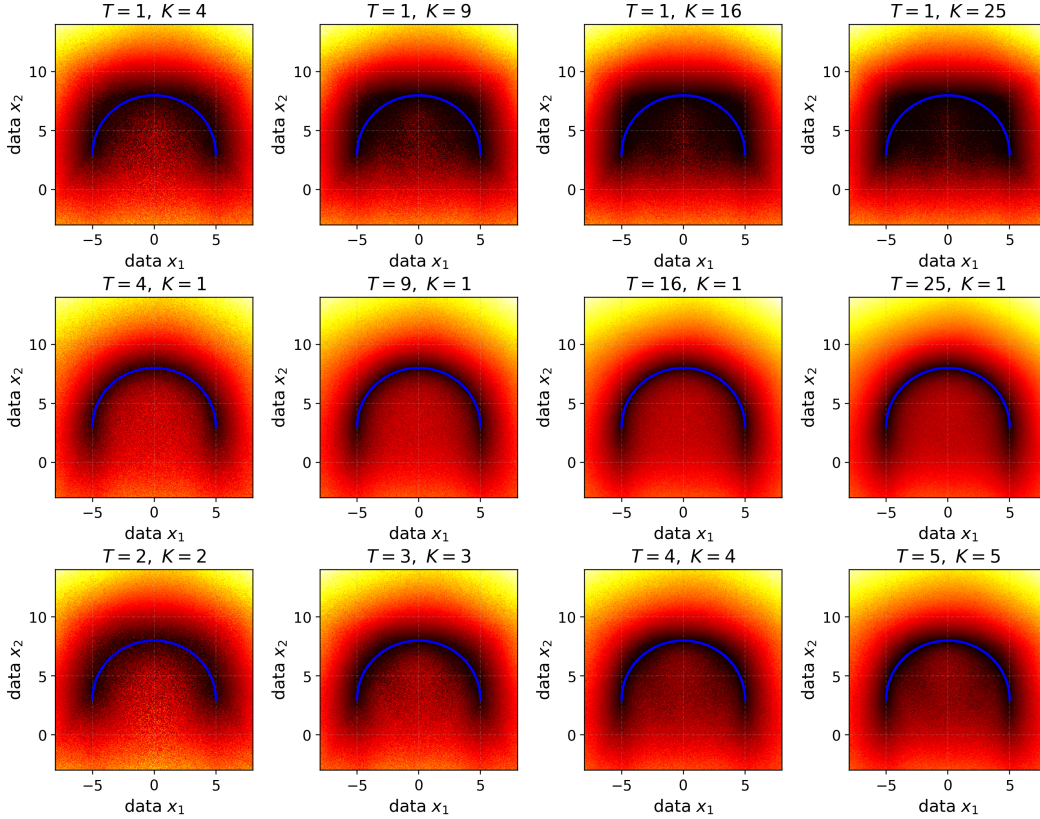


Figure 5: Half-moon toy analysis: anomaly score maps under different (T, K) settings. Larger T and K reduce sampling artifacts and produce smoother, more stable score maps.

B.2 Toy example 2: visualization of the time weighting effect on anomaly scores.

In this toy example, we show the time weighting behaviors on the geometry-constrained setting. The normal data distribution is supported on the upper semicircle, while the source distribution is a two-dimensional standard Gaussian. We train a time-conditioned MLP flow-matching model and evaluate mismatch score maps on a dense grid. For each grid point p , we compute path-wise residuals across Gaussian draws and aggregate them using the minimum across paths (Eq. 3), then aggregate over time using Eq. 4 with $w(t) = t^2$.

Figure 6 visualizes per-time mismatch maps and their weighted combination. At small t , interpolation states are dominated by source noise, so the map shows stronger global bias and weaker geometric localization. At larger t , localization around the half-moon manifold becomes sharper, but estimates are also more variable. The weighted combination with $w(t) = t^2$ balances these effects by emphasizing informative later times while still integrating over the full trajectory, producing a smoother and more stable final score map.

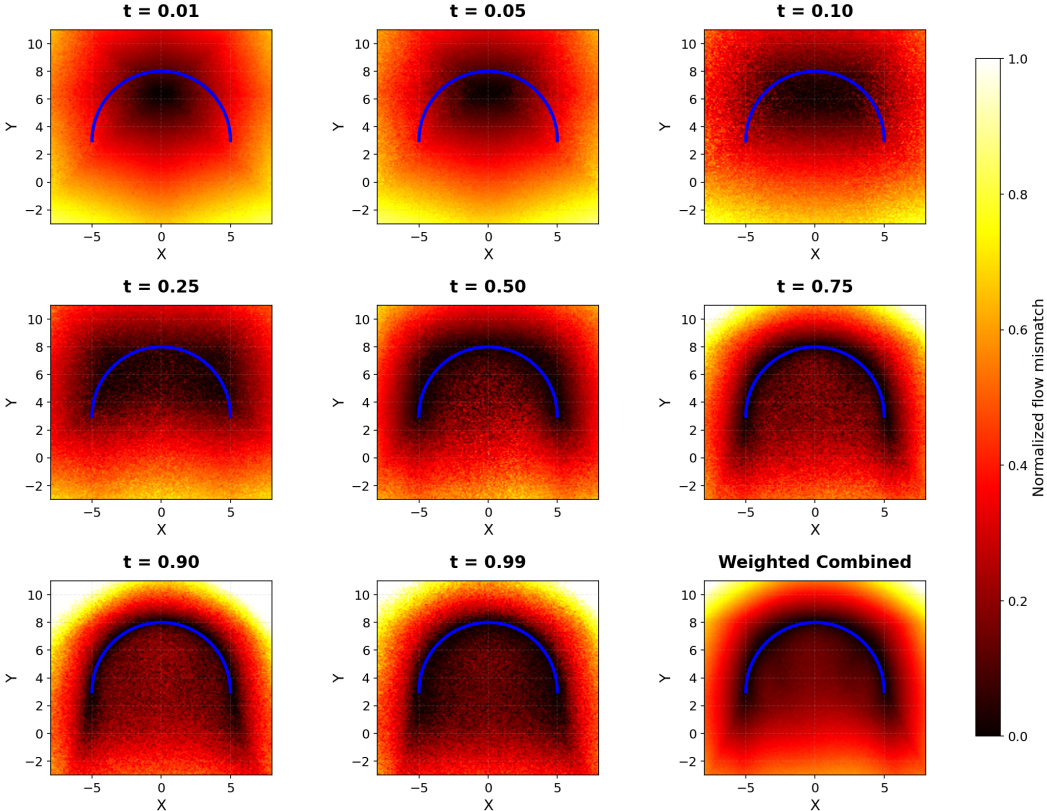


Figure 6: Toy example 2: time-dependent flow mismatch score maps and weighted aggregation.

B.3 Toy example 3: visualization of flow mismatching under a pooled categories setting.

In this toy example, we further illustrate how Flow Mismatching behaves when normal data are pooled from several categories. In high-dimensional spaces, normal samples are rarely unimodal. Instead, they form multiple clusters corresponding to different normal modes. A flow-matching model trained on pooled normal data learns a velocity field over the entire space, and from a given state it tends to move toward a nearby plausible normal cluster.

This pooled-category structure does not invalidate the mismatch signal because each test path is anchored at the same endpoint y . For a normal target, y belongs to one of the valid normal clusters. Although early-time mismatch may be affected by interference among clusters, the mismatch decreases as the path approaches the target cluster, where the learned flow velocity becomes more consistent with the affine transport velocity. The t^2 weighting further suppresses early-time discrepancies, yielding a stable aggregated score.

Path aggregation provides an additional stabilizing effect. Since different seeds x_0 may induce different transient trajectories, aggregating over multiple paths reduces sensitivity to any individual seed and preserves mismatch patterns that are consistent across paths. This agrees with the empirical trend that increasing path and time scaling improves stability.

For visualization, we consider a toy example with 3 normal clusters and compare affine paths from $(0, 0)$, $(-2, -4)$, and $(2, 0)$ to both a normal target and an anomalous target. We plot the

mismatch scores before and after applying the t^2 weighting along each path. The results show that for anomalous targets outside the pooled normal support, the learned flow velocity tends to point toward nearby normal clusters, whereas the affine transport velocity points directly toward the target. This disagreement produces a large flow mismatch. In contrast, for normal targets, the two velocities become increasingly aligned as the path approaches the corresponding normal cluster.

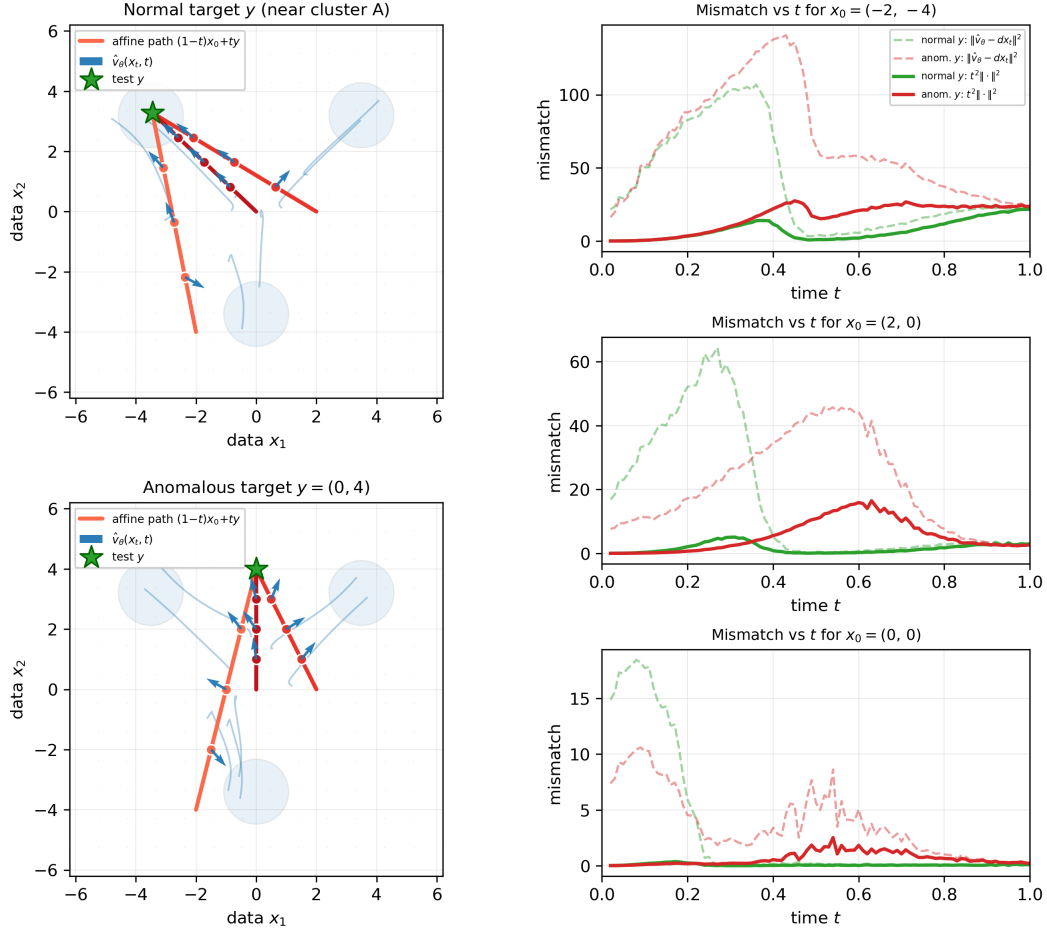


Figure 7: Toy example 3: flow mismatching under a pooled category case.

C Implementation Details

C.1 Flow Matching U-Net Architecture

We parameterize the velocity field $v_\theta(x_t, t)$ using a time-conditioned attention U-Net [Lipman et al., 2024]. The model takes a 3-channel image as input and predicts a 3-channel velocity field at the same spatial resolution. By default, we use 64 base channels, 3 residual blocks per level, channel multipliers (1, 1, 2, 2, 4, 4), attention downsample rates (4, 8, 16, 32), 32 channels per attention head, and dropout rate 0.05. The network uses residual up/downsampling blocks, scale-shift normalization, and the new QKV attention ordering. For 128×128 inputs, this configuration produces feature maps with channels 64, 64, 128, 128, 256, 256 at resolutions 128, 64, 32, 16, 8, 4, respectively. The attention resolutions are specified as downsample rates rather than absolute spatial sizes, so self-attention is applied at the 32×32 , 16×16 , 8×8 , and 4×4 feature maps. The middle block additionally includes one attention layer at the bottleneck.

Each residual block consists of group normalization, SiLU activation, 3×3 convolutions, timestep-conditioned scale-shift modulation, and dropout. The scalar time t is embedded using sinusoidal features and passed through a two-layer MLP of dimension $64 \rightarrow 256 \rightarrow 256$. The resulting embedding conditions every residual block. Attention uses a fixed head width of 32 channels, giving 4 heads at 128 channels and 8 heads at 256 channels. The encoder contains six resolution stages, each with three residual blocks, and downsamples the input to a 4×4 bottleneck. The decoder mirrors the encoder and concatenates the corresponding encoder activations through U-Net skip connections. A final group normalization, SiLU activation, and zero-initialized 3×3 convolution produce the predicted velocity $v_\theta(x_t, t)$. We use this relatively lightweight backbone because Flow Mismatching evaluates the velocity model multiple times per image across sampled paths and time steps. The 64-channel U-Net provides a favorable speed-accuracy tradeoff while retaining multi-scale semantic context through low-resolution attention.

We train the flow model using the standard flow-matching regression objective with affine interpolants $x_t = (1-t)x_0 + tx_1$ and target velocity $x_1 - x_0$. The network is optimized with StableAdamW using AMSGrad, learning rate 10^{-4} , weight decay 10^{-4} , betas (0.9, 0.99), and $\epsilon = 10^{-6}$. We use update RMS clipping with threshold 1.0; additional gradient-norm clipping is disabled by default. Training uses mixed precision with bfloat16, TF32 acceleration, batch size 32, image resolution 128×128 , and gradient accumulation step 1. The default training runs for 2000 epochs with distributed data parallelism, using class-conditional labels when available.

C.2 Details for the compared Flow Matching-based methods

We group flow-matching (FM) baselines into: (i) *training-modified* methods that change the FM objective, and (ii) *inference-only* methods that keep vanilla FM training but alter test-time inference. For fairness, all methods use the same backbone architecture and optimizer as our default setting, and no extra feature extractor is applied. For the three inference-only methods D-Flow, ReconFlow, and Flow Mismatching, they are evaluated using the same trained flow model. Per-class metrics comparison is shown in Appendix E.

Reflect (training-modified). Reflect [Beizae et al., 2025] trains a rectified-flow that maps a *synthetically corrupted* (pseudo-abnormal) sample back to its clean normal counterpart. Given a normal latent y_1 and a binary mask $m \in \{0, 1\}^{H \times W}$, Reflect forms a corrupted sample

$$y_0 = (\sqrt{1-\alpha}y_1 + \sqrt{\alpha}r) \odot m + y_1 \odot (1-m), \quad \alpha \sim \mathcal{U}[0, 1], \quad (14)$$

where r is a replacement vector,

$$r = \sqrt{\beta}q + \sqrt{1-\beta}p, \quad (15)$$

where $q \in \mathbb{R} \sim \mathcal{N}(0, 1)$ is a scalar, $p \in \mathbb{R}^{H \times W} \sim \mathcal{N}(0, \mathbf{I})$ is spatial i.i.d. Gaussian noise, and $\beta \sim \mathcal{U}[0, 1]$. All channels are sampled independently. To synthesize realistic, irregular anomaly shapes, Reflect generates up to N non-overlapping binary masks $\{m_i\}_{i=1}^N$. Each mask $m_i \in \{0, 1\}^{H \times W}$ is produced by a 2D random walk: starting from a uniformly sampled seed pixel, take a random number of steps, where at each step the walk moves to one of the (4- or 8-connected) neighboring pixels with equal probability. The masked region corresponds to the set of visited pixels during the walk;

multiple regions are enforced to be non-overlapping. We followed the same mask generation strategy as their official implementation.

Training follows standard rectified FM with linear interpolants $y_t = (1 - t)y_0 + ty_1$ and constant target velocity, with the pair (y_0, y_1) .

$$\min_{\theta} \mathbb{E}_{t \sim \mathcal{U}[0,1]} \left[\left\| (y_1 - y_0) - v_{\theta}(y_t, t) \right\|_2^2 \right]. \quad (16)$$

At test time, given the test image y_{test}^0 , Reflect used a one-step generation to get the ‘‘anomaly-free’’ reconstruction,

$$y_{test}^1 = y_{test}^0 - v_{\theta}(y_{test}^0, 0), \quad (17)$$

and therefore we used $\| -v_{\theta}(y_{test}^0, 0)(p) \|_2$ as the anomaly heatmap.

TCCM (training-modified). TCCM [Li et al., 2025b] learns a *time-conditioned contraction* vector field that contracts normal samples toward the origin. Instead of transporting Gaussian noise to data, the velocity is supervised toward the contraction direction:

$$v_{\theta}(x, t) \approx -x, \quad (18)$$

for t across all time. Following the paper, we train a time-conditioned contraction field by minimizing

$$\min_{\theta} \mathbb{E}_{x \sim p_{\text{data}}, t \sim \mathcal{U}(0,1)} \left[\left\| v_{\theta}(x, t) + x \right\|_2 \right]. \quad (19)$$

At test time with test image y , anomaly heatmap is computed from the contraction residual at a fixed time (default $t = 1$):

$$\left\| v_{\theta}(y, t) + y \right\|_2, \quad t_{\text{fixed}} = 1. \quad (20)$$

Remarkably, TCCM is not initially developed for visual anomaly localization. We also found the training objective is very likely to yield an overfitting model that outputs exactly $-y$ for even an anomalous sample y , thus giving a trivial heatmap that has no effect. To avoid this issue, we only trained 50 epochs on the whole dataset for TCCM.

WT-Flow (training-modified). WT-Flow [Li et al., 2025a] trains a *reverse* rectified-flow that transports normal samples toward a standard Gaussian and detects anomalies via a Gaussian density proxy at the transported endpoint. In the original method, the flow is learned in a frozen WRN-50 feature space; in our implementation, we remove the feature extractor and apply WT-Flow directly in the *image domain*.

Given an input image (or tensor) $x \in \mathbb{R}^{C \times H \times W}$, WT-Flow applies the non-learnable affine normalization

$$\text{WT}(x) = \gamma x + \beta, \quad \gamma = \frac{1}{\sqrt{\sigma^2 + \epsilon}}, \quad \beta = -\frac{\mu}{\sqrt{\sigma^2 + \epsilon}}, \quad (21)$$

where μ, σ denote the (per-sample) mean and standard deviation of x , and ϵ is a small constant. This corresponds to standardizing each sample before transport.

Let x_0 be a normal training image and $x_0'' = \text{WT}(x_0)$ its WT-mapped version. $x_1 \sim \mathcal{N}(0, \mathbf{I})$ with the same shape as x_0'' , draw $t \sim \mathcal{U}[0, 1]$, and define the linear interpolant

$$x_t = (1 - t)x_0'' + tx_1. \quad (22)$$

We train a time-dependent velocity field v_{θ} using the rectified-flow regression loss following their paper.

$$\min_{\theta} \mathbb{E}_{t \sim \mathcal{U}[0,1]} \left[\left\| (x_1 - x_0'') - v_{\theta}(x_t, t) \right\|_2^2 \right]. \quad (23)$$

Given a test image y , we first compute $y'' = \text{WT}(y)$ and then integrate the learned flow ODE from $t = 0$ to 1 (‘‘backward sampling’’) starting at y'' ,

$$\hat{x}_1 = \text{ODE}(y'', v_{\theta}). \quad (24)$$

then form a pixel-wise Gaussian density proxy from the transported endpoint. Concretely, the Gaussian energy is used as the anomaly heatmap:

$$E(p) = \frac{1}{2} \sum_{c=1}^C \hat{x}_1(p, c)^2, \quad (25)$$

which is proportional to $-\log p(\hat{x}_1(p))$ under a standard Gaussian.

D-Flow accelerated by FlowGrad (inference-only). D-Flow [Ben-Hamu et al., 2024] performs *test-time optimization* over the flow’s initial condition (or latent) to reconstruct a given observation. Let Φ_θ denote the flow/ODE solution map from x_0 to x_1 (endpoint after integration). D-Flow solves:

$$\hat{x}_0 = \arg \min_{x_0} \mathcal{L}(\Phi_\theta(x_0), y), \quad (26)$$

where \mathcal{L} is a guidance loss (we use MSE), y is the given test image. We run gradient-based optimization to obtain $\hat{x}_1 = \Phi_\theta(\hat{x}_0)$ and use reconstruction residuals as the anomaly heatmap,

$$h(i) = \|y(i) - \hat{x}_1(i)\|_2. \quad (27)$$

Vanilla D-Flow is very slow in solving the optimization problem. To reduce the cost of backpropagating through ODE integration, we adopt FlowGrad [Liu et al., 2023a], which provides an efficient gradient computation scheme for guided flow sampling and supports fewer/selected discretization steps when the trajectory is locally straight.

ReconFlow (ours, inference-only reconstruction baseline). ReconFlow is a reconstruction-style counterpart of our method. it keeps *vanilla* FM training (same objective and backbone as our model) and only changes test-time inference to output an explicit reconstruction \hat{y} of the test image. In specific,

$$y_t = (1 - t_{\text{init}})x_0 + t_{\text{init}}y, \quad x_0 \sim \mathcal{N}(0, \mathbf{I}), \quad \hat{y} = \Phi_\theta(y_t, t_{\text{init}}). \quad (28)$$

We then define the pixel-level heatmap:

$$h(i) = \|y(i) - \hat{y}(i)\|_2. \quad (29)$$

For fairness and consistency with Flow Mismatching, we set $t_{\text{init}} = 0.5$, and also sample $K = 10$ noise x_0 , and the integration steps $T = 10$ in $\hat{y} = \Phi_\theta(y_t, t_{\text{init}})$. The final heatmap takes minimum over the $K = 10$ reconstructed image.

D Additional Experiments and Discussion

D.1 Training epochs.

In our default setting, we train the flow matching model for 2000 epochs. This choice is intended to ensure that the model sufficiently learns the normal-data dynamics, so that the learned velocity field is a faithful approximation of the normal generative flow assumed in our theory. To investigate whether longer training improves this approximation or instead causes overfitting to the normal training set, we evaluate checkpoints from epoch 100 to epoch 2000 with the same inference setting. The results in Figure 8 show a clear convergence pattern. At early epochs, the learned velocity field is still under-trained, leading to noticeably weaker image-level detection and pixel-level localization. As training proceeds, all three mean metrics improve, indicating that a better normal-flow estimate produces a stronger and more reliable velocity-mismatch signal. We do not observe the typical signature of harmful overfitting, namely a late-epoch drop in anomaly detection or localization performance. Instead, the 2000 epoch checkpoint lies on the stable high-performance plateau, supporting its use as the default model. See detailed results in Table 9.

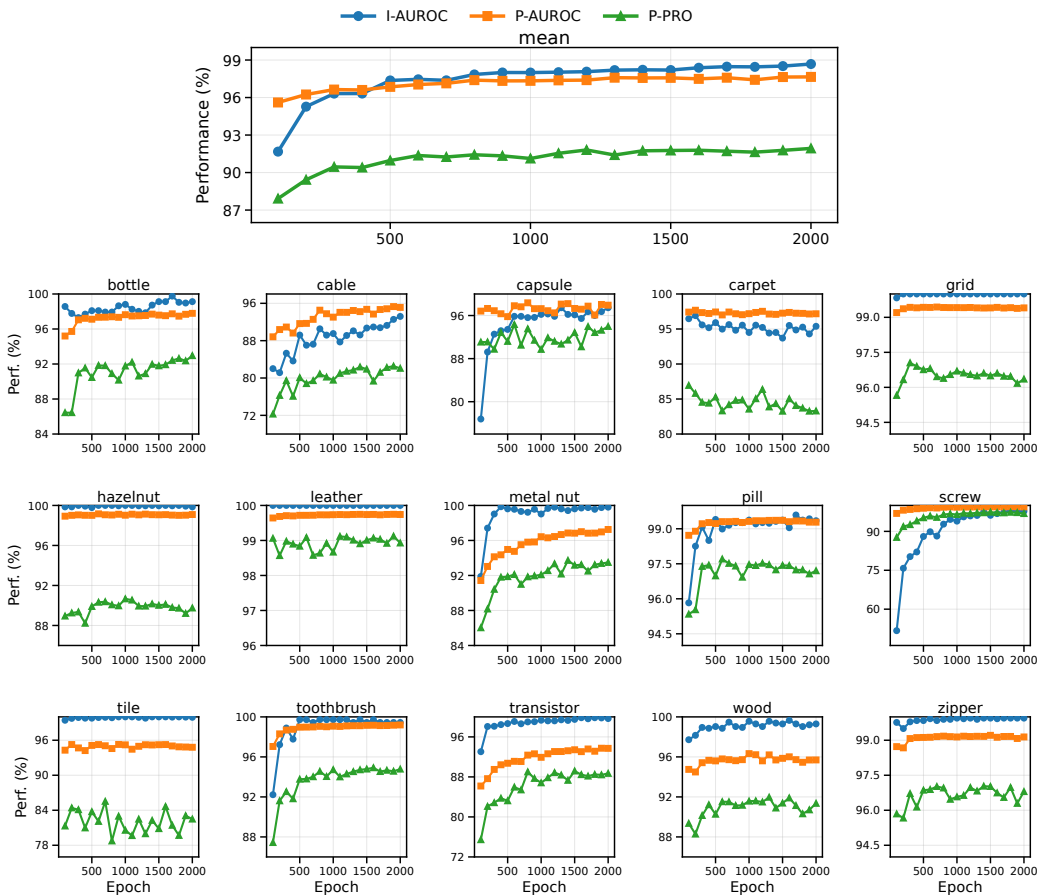


Figure 8: Training-epoch ablation on MVTEC-AD. We evaluate checkpoints from epoch 100 to epoch 2000 under a fixed inference budget. The top panel shows the mean performance, while the remaining panels show per-category trends. I-AUROC, P-AUROC, and P-PRO improve rapidly at early epochs and then plateau, suggesting that longer training yields a more reliable normal-flow estimate without evident overfitting.

D.2 Failure Case Analysis

The main failure cases of Flow Mismatching occur on large object-level anomalies. As shown in the qualitative results, our method is effective at localizing small defects and fine-grained appearance

changes. However, when the anomaly occupies a large semantic region, Flow Mismatching may fail to cover the entire anomalous area and instead highlight only its boundaries. See Figure 9.

A possible explanation is that large object-level anomalies are often caused by semantic or logical discrepancies rather than purely local appearance changes. Since our current flow matching model is evaluated directly in pixel space, its representation capacity is biased toward local texture and boundary-level differences, while its ability to capture high-level semantic inconsistency is limited. This suggests that incorporating stronger semantic representations, more advanced architectures, or latent-space flow formulations may further improve performance on large structural anomalies.

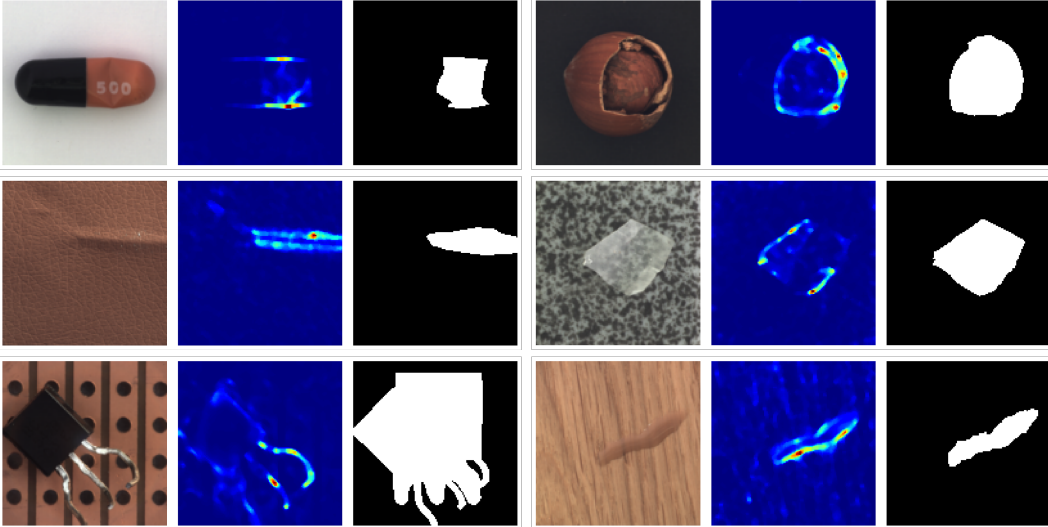


Figure 9: Failure cases of our method.

D.3 Limitation.

In our perspective, there are three main limitations of the current work.

First, Flow Mismatching requires $O(KT)$ forward evaluations per test image, where K is the number of sampled paths and T is the number of time steps. Thus, its throughput depends directly on the chosen test-time compute budget. To make this trade-off explicit, we report performance across different (K, T) settings, showing how accuracy improves with additional path/time evaluations and enabling practitioners to choose an appropriate operating point depending on their latency and accuracy requirements. Also, in Table 3 we show that our method’s FPS is within a reasonable range compared with other SOTAs.

Second, our theoretical interpretation also assumes that the learned flow is a good approximation of the oracle normal flow. If the model is under-trained, misspecified, or insufficiently expressive, the resulting score gap may no longer cleanly reflect the population-level Fisher-divergence signal. Empirically, we partially address this issue by reporting epoch–performance curves, which show how detection performance evolves as training progresses. From the results, training successfully recovers the target normal-path distribution. Moreover, recent universal approximation theoretical guarantee Zhou and Liu [2025] also supports that flow matching model itself is capable of approximating the oracle velocity field within small enough error.

Finally, our experiments focus on industrial anomaly benchmarks at moderate image resolutions. Scaling Flow Mismatching to substantially larger images may increase both memory usage and inference cost, especially because the method evaluates multiple paths and time steps. In ongoing work, we are exploring more advanced architectures and latent-space flow formulations, which can reduce the computational burden and make the approach more practical for higher-resolution settings and faster inference.

E Detailed Tables and Figures in Experiments

Table 3: Efficiency comparison of industrial anomaly detection baselines. Params and FLOPs are collected from literature-reported or benchmark-reported sources and may not be strictly comparable across methods due to differences in backbone inclusion, image resolution, FLOP-counting conventions, hardware, and batch size. FPS is either self-implemented, reported, or converted from reported inference time when available.

Method	Params	FLOPs	FPS
CFLOW-AD [Gudovskiy et al., 2022]	237M	28.7G	30.8
RD4AD [Deng and Li, 2022]	80.6M	28.4G	4.82
UniAD [You et al., 2022]	24.5M	3.4G–3.6G	5.29
SimpleNet [Liu et al., 2023b]	72.8M	16.1G–17.7G	4.93
DeSTSeg [Zhang et al., 2023]	35.2M	30.7G–122.7G	90.8
HVQ-Trans [Lu et al., 2023]	18.0M [†]	7.38G [†]	5.57
DiAD [He et al., 2024a]	1331M	451.5G->2.2T	1.64
MambaAD [He et al., 2024b]	25.7M	8.3G	50.7
ViTAD [Zhang et al., 2025b]	39.0M	9.7G	115.0
AMDM / OmiAD [Feng et al., 2025]	–	–	39.37
D-Flow [Ben-Hamu et al., 2024]	–	–	0.07
Flow Mismatching ($K = T = 5$)	45.3M	25.3G	15.92
Flow Mismatching (<i>default</i>)	45.3M	25.3G	3.87

[†] For HVQ-Trans, reported parameters/FLOPs exclude the backbone in the available source. For AMDM/OmiAD, only FPS was found from the accessible source; Params and FLOPs were not reported. D-Flow is an inference only method, and implemented with the same model as ours, so only the model FPS is reported.

Table 4: Per-class image-level comparison of flow-matching-based methods on MVTec-AD. Each entry reports AUROC/AP/ F_1 -max. Best values are shown in **bold**.

Category	Training-modified FM			Inference-only FM		
	Reflect MICCAI'25	TCMM NeurIPS'25	WT-Flow	D-Flow ICML'24	ReconFlow	Ours
<i>Image-level metrics: AUROC/AP/F_1-max</i>						
bottle	60.2/86.4/86.3	28.3/66.9/86.3	84.4/95.4/87.0	92.5/97.8/92.4	98.3/99.5/ 98.4	99.1/99.7/97.6
cable	67.8/78.8/76.0	36.8/57.9/76.0	62.6/73.7/76.5	67.8/73.2/78.1	85.9/91.0/83.7	93.2/96.6/90.8
capsule	36.5/80.2/90.5	49.2/84.1/90.5	95.9/99.1/96.0	70.0/91.6/91.6	80.9/95.2/91.6	97.4/99.5/96.4
carpet	55.8/83.1/86.4	25.3/67.3/86.4	80.1/92.1/90.8	57.1/83.5/86.4	80.7/93.8/87.9	95.4/98.7/93.0
grid	59.8/81.9/84.6	67.3/86.3/84.8	99.7/99.9/99.1	70.9/83.8/85.9	100/100/100	100/100/100
hazelnut	84.4/91.8/82.4	92.9/96.4/89.5	98.1/98.3/97.2	89.8/94.2/87.1	99.4/99.7/97.8	99.9/99.9/99.3
leather	85.9/95.8/86.6	65.4/88.7/85.2	97.9/99.2/96.8	97.4/99.1/95.0	99.5/99.8/98.3	100/100/100
metal_nut	52.4/87.0/89.4	49.8/79.5/90.3	89.0/97.4/91.8	62.0/85.6/89.9	94.3/98.6/94.6	99.8/100/99.5
pill	68.7/92.8/91.9	67.5/93.0/91.9	78.3/95.5/92.2	62.4/90.9/91.9	70.1/92.4/93.3	99.3/99.9/98.9
screw	78.0/91.2/87.1	8.4/55.3/85.3	60.2/82.7/85.3	44.6/71.8/85.9	92.6/96.9/94.0	97.8/99.2/96.7
tile	74.8/90.2/83.6	66.1/84.2/84.7	99.8/99.9/98.8	72.9/88.3/86.2	91.3/97.0/90.7	99.9/100/99.4
toothbrush	73.6/88.7/87.5	61.9/84.5/84.1	90.8/96.2/91.5	98.6/99.4/96.8	99.7/99.9/98.4	99.4/99.8/98.4
transistor	64.3/67.6/59.1	41.2/42.3/57.8	75.9/68.9/69.3	81.5/77.8/74.5	99.2/98.9/96.2	99.7/99.6/97.5
wood	85.1/96.0/89.5	96.4/99.0/94.9	99.1/99.7/98.3	94.7/98.3/94.3	96.8/99.0/94.9	99.3/99.8/98.4
zipper	48.9/83.1/88.1	47.6/80.9/88.1	62.8/86.8/90.2	67.1/86.0/88.8	87.7/96.0/95.2	99.9/100/99.6
Mean	66.4/86.3/84.6	53.6/77.7/85.1	85.0/92.3/90.7	75.3/88.1/88.3	91.8/97.2/94.3	98.7/99.5/97.7

Table 5: Per-class pixel-level comparison of flow-matching-based methods on MVTec-AD. Each entry reports AUROC/AP/ F_1 -max/AUPRO. Best values are shown in **bold**.

Category	Training-modified FM			Inference-only FM		
	Reflect MICCAI'25	TCMM NeurIPS'25	WT-Flow	D-Flow ICML'24	ReconFlow	Ours
<i>Pixel-level metrics: AUROC/AP/F_1-max/AUPRO</i>						
bottle	59.9/17.4/25.0/20.4	68.8/15.8/26.3/29.4	76.9/22.9/30.5/41.0	91.4/57.7/56.8/55.2	93.1/63.8/61.7/49.7	97.8/76.8/69.9/93.0
cable	51.1/13.6/20.2/26.0	52.9/9.9/16.9/25.4	61.3/16.6/23.4/35.8	85.3/27.2/35.6/57.7	85.6/39.3/43.1/59.5	95.1/51.8/51.3/82.1
capsule	40.5/6.3/9.2/23.6	83.3/16.1/23.2/71.8	95.9/ 58.5/62.1/90.2	92.0/34.0/38.9/70.4	94.6/43.1/48.1/81.6	97.9/48.5/51.5/94.0
carpet	70.2/16.3/21.6/39.6	55.6/9.7/14.4/30.8	90.9/61.2/61.5/80.7	79.3/21.1/26.2/52.3	87.9/41.3/45.6/71.6	97.2/70.0/67.6/83.3
grid	74.3/15.5/22.6/51.5	61.4/2.4/6.1/29.2	97.6/ 56.6/60.2/93.2	62.8/8.5/12.1/27.6	96.0/49.7/53.5/83.9	99.4/55.7/55.1/96.4
hazelnut	70.6/31.9/35.8/33.5	97.3/70.5/70.2/87.7	96.8/79.4/ 79.1/87.0	97.2/63.9/62.2/82.3	98.7/79.9/77.4/84.7	99.1/69.2/70.1/89.7
leather	79.0/41.1/45.7/55.3	79.6/40.5/45.7/65.5	97.1/ 76.0/75.0/91.1	98.4/68.9/69.8/94.3	98.9/66.2/67.2/92.4	99.7/68.8/66.9/98.9
metal_nut	53.3/26.7/34.9/28.3	79.5/34.6/40.1/47.4	71.0/50.0/55.6/55.1	89.3/41.7/48.1/54.8	96.5/75.3/75.0/71.2	97.3/85.5/79.1/93.5
pill	58.4/19.9/24.2/37.7	88.1/25.1/31.0/63.3	79.5/31.7/36.2/56.5	95.7/40.0/46.6/75.9	96.4/45.7/51.4/83.7	99.3/84.2/77.3/97.2
screw	39.3/0.5/1.4/14.6	90.8/3.6/8.9/70.9	96.8/11.3/22.2/88.7	92.3/17.8/22.7/73.6	95.4/46.1/50.7/82.2	99.4/55.3/54.1/96.9
tile	75.8/41.8/46.2/41.4	60.1/31.9/37.0/40.4	91.0/73.6/ 72.5/81.6	68.7/27.7/34.4/40.7	76.4/45.6/47.5/51.2	94.8/74.4/68.1/82.5
toothbrush	68.3/13.8/18.7/34.2	88.4/14.2/21.1/62.3	83.1/29.0/38.4/65.5	97.9/60.9/61.0/85.1	98.8/62.0/63.1/86.6	99.2/63.5/65.4/94.8
transistor	44.6/15.7/24.1/15.6	50.2/14.5/22.5/25.2	61.6/24.1/30.3/34.4	85.3/34.7/38.5/58.5	87.1/53.5/55.4/61.0	93.7/58.1/56.1/88.7
wood	67.2/23.9/30.0/33.8	78.3/48.0/51.3/66.1	89.9/ 71.3/70.5/79.8	79.9/35.5/38.1/55.3	86.8/48.6/50.0/66.9	95.7/70.9/65.4/91.4
zipper	50.1/8.3/13.7/18.9	61.3/9.4/17.5/32.9	91.0/36.0/41.7/72.1	91.1/24.0/36.5/50.3	94.3/47.4/52.0/63.8	99.1/79.3/74.2/96.8
Mean	60.2/19.5/24.9/31.6	73.0/23.1/28.8/49.9	85.4/46.5/50.6/70.2	87.1/37.6/41.8/62.3	92.4/53.8/56.1/72.7	97.7/67.5/64.8/91.9

Table 6: Test-time compute ablation on MVTEC-AD. We report mean results over the 15 categories. All values except FPS are percentages. Best values within each setting are shown in bold.

Ablation	Setting	KT	Image-level			Pixel-level				FPS
			AUROC	AP	F1-max	AUROC	AP	F1-max	PRO	
<i>Fix $K = 5$, vary T</i>										
	$T = 2$	10	97.9	99.3	96.8	96.2	63.4	61.7	89.9	37.48
	$T = 4$	20	98.1	99.3	97.2	96.9	65.5	63.2	90.3	18.85
	$T = 6$	30	98.2	99.4	97.3	97.1	65.9	63.5	91.1	12.56
	$T = 8$	40	98.2	99.3	97.5	97.2	66.3	63.7	91.0	9.42
	$T = 10$	50	98.2	99.3	97.4	97.2	66.4	63.9	91.5	7.56
	$T = 12$	60	98.2	99.3	97.3	97.3	66.7	64.1	91.2	6.31
	$T = 14$	70	98.2	99.3	97.4	97.3	66.8	64.1	91.4	5.40
	$T = 16$	80	98.1	99.2	97.1	97.3	66.8	64.2	91.3	4.73
	$T = 18$	90	98.3	99.4	97.2	97.3	66.9	64.2	91.2	4.20
	$T = 20$	100	98.2	99.3	97.3	97.3	66.9	64.3	91.0	3.78
<i>Fix $T = 5$, vary K</i>										
	$K = 2$	10	96.2	98.5	95.7	96.1	62.8	60.6	88.9	34.96
	$K = 4$	20	97.8	99.2	97.1	96.8	65.3	62.9	90.3	18.61
	$K = 6$	30	98.4	99.4	97.4	97.1	66.2	63.8	91.0	12.61
	$K = 8$	40	98.5	99.4	97.6	97.3	66.5	64.1	91.4	9.60
	$K = 10$	50	98.6	99.5	97.6	97.4	66.7	64.1	91.3	7.73
	$K = 12$	60	98.6	99.5	97.8	97.5	66.8	64.3	91.6	6.46
	$K = 14$	70	98.7	99.5	97.7	97.5	66.9	64.3	91.8	5.55
	$K = 16$	80	98.7	99.5	97.9	97.6	67.0	64.4	92.0	4.87
	$K = 18$	90	98.7	99.5	97.7	97.6	67.1	64.5	92.0	4.33
	$K = 20$	100	98.8	99.6	97.8	97.6	67.1	64.5	91.8	3.90
<i>Joint $K = T$</i>										
	$K = T = 2$	4	95.9	98.5	95.5	95.4	60.5	58.9	87.7	86.40
	$K = T = 4$	16	97.8	99.2	97.2	96.7	65.0	62.8	90.4	23.11
	$K = T = 6$	36	98.3	99.4	97.3	97.2	66.3	63.8	91.1	10.51
	$K = T = 8$	64	98.6	99.5	97.4	97.5	67.1	64.5	91.5	6.01
	$K = T = 10$	100	98.7	99.5	97.7	97.7	67.5	64.8	91.9	3.87
	$K = T = 12$	144	98.7	99.5	97.7	97.7	67.6	64.9	92.2	2.70
	$K = T = 14$	196	98.7	99.5	97.8	97.8	67.8	65.1	92.2	1.99
	$K = T = 16$	256	98.8	99.5	97.7	97.8	67.8	65.1	92.2	1.53
	$K = T = 18$	324	98.8	99.5	97.7	97.9	68.0	65.3	92.2	1.20
	$K = T = 20$	400	98.8	99.5	97.8	97.9	67.9	65.2	92.3	0.98



Figure 10: Per-category ablation on MVTEC-AD with fixed $K = 5$ and varying number of time steps T . Each panel reports I-AUROC, P-AUROC, and P-PRO; the Mean panel additionally shows FPS.



Figure 11: Per-category ablation on MVTEC-AD with fixed $T = 5$ and varying number of paths K . Each panel reports I-AUROC, P-AUROC, and P-PRO; the Mean panel additionally shows FPS.

Table 7: Ablation on path aggregation for Flow Mismatching. We report mean results over categories on MVTEC-AD and VisA. Best values within each dataset and metric are shown in bold.

Aggregator	Image-level			Pixel-level			
	AUROC	AP	F1-max	AUROC	AP	F1-max	PRO
<i>MVTec-AD</i>							
Average	94.4	97.6	95.0	94.9	60.4	58.3	87.7
q_{30} quantile	97.5	99.0	96.8	96.3	65.2	62.6	90.2
q_{20} quantile	98.0	99.2	97.1	96.7	66.2	63.6	91.1
q_{10} quantile	98.4	99.4	97.3	97.0	67.0	64.2	91.5
Minimum (default)	98.7	99.5	97.7	97.7	67.5	64.8	91.9
<i>VisA</i>							
Average	96.7	97.8	93.4	94.4	39.0	45.3	85.5
q_{30} quantile	97.9	98.5	94.9	96.8	40.7	46.5	89.4
q_{20} quantile	97.9	98.5	94.9	97.2	40.9	46.6	89.9
q_{10} quantile	97.8	98.3	94.7	97.4	40.7	46.2	90.5
Minimum (default)	98.0	98.4	95.2	97.5	40.2	45.8	90.6

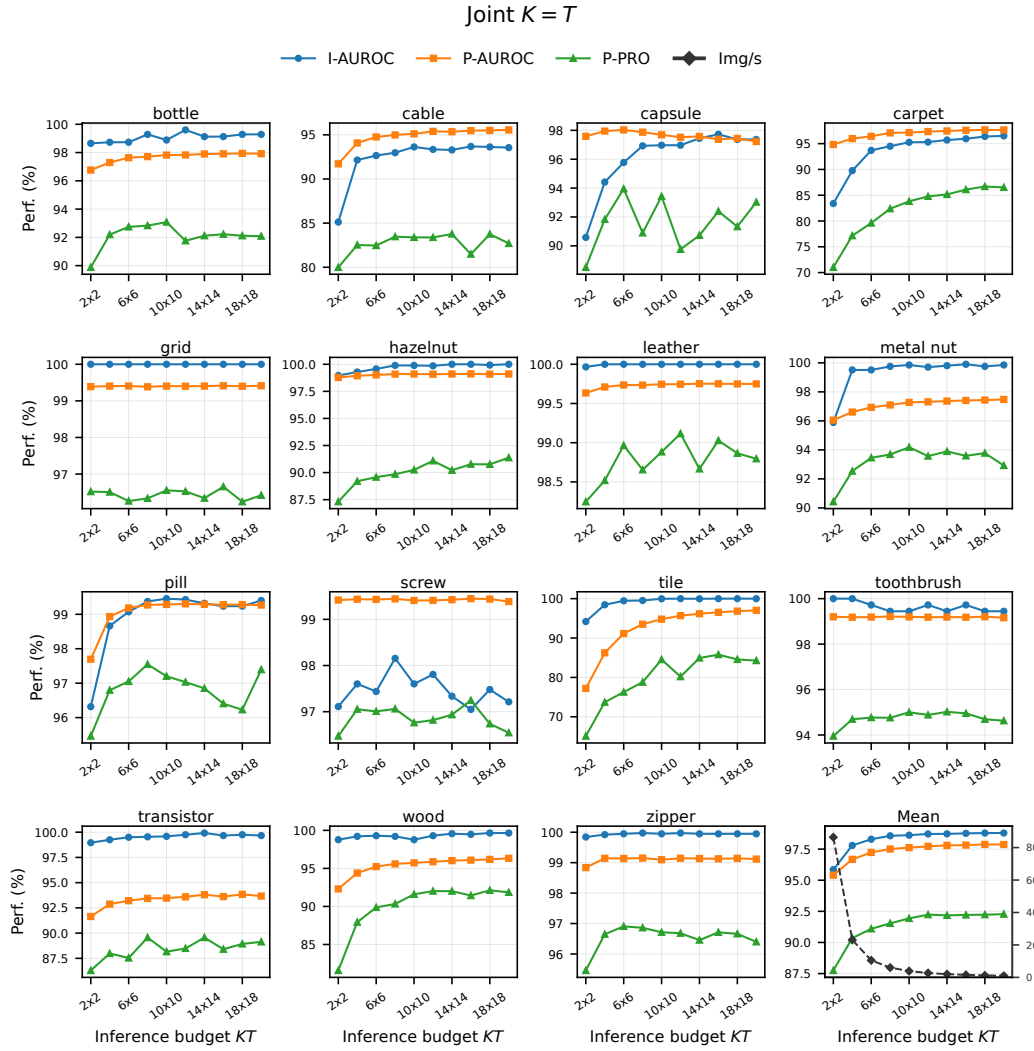


Figure 12: Per-category ablation on MVTEC-AD under joint test-time compute scaling with $K = T$. Each panel reports I-AUROC, P-AUROC, and P-PRO; the Mean panel additionally shows FPS.

Table 8: Ablation on pooled categories vs. condition label training on MVTec-AD and VisA.

Class	Pooled categories training							Conditional category label training(<i>default</i>)						
	Image-level			Pixel-level				Image-level			Pixel-level			
	AUROC	AP	F_1 -max	AUROC	AP	F_1 -max	PRO	AUROC	AP	F_1 -max	AUROC	AP	F_1 -max	PRO
MVTec-AD														
bottle	98.5	99.6	98.4	96.8	72.6	65.1	90.5	99.1	99.7	97.6	97.8	76.8	69.9	93.0
cable	91.8	95.9	90.7	92.8	43.4	43.0	78.0	93.2	96.6	90.8	95.1	51.8	51.3	82.1
capsule	92.6	98.4	94.6	97.1	49.1	50.6	93.1	97.4	99.5	96.4	97.9	48.5	51.5	94.0
carpet	96.8	99.1	94.8	97.0	68.5	66.5	87.8	95.4	98.7	93.0	97.2	70.0	67.6	83.3
grid	100	100	100	99.4	59.7	58.3	96.5	100	100	100	99.4	55.7	55.1	96.4
hazelnut	100	100	100	99.1	71.0	70.9	89.6	99.9	99.9	99.3	99.1	69.2	70.1	89.7
leather	100	100	100	99.7	68.6	68.5	99.1	100	100	100	99.7	68.8	66.9	98.9
metal_nut	99.7	99.9	98.9	93.4	75.5	69.0	90.4	99.8	100.0	99.5	97.3	85.5	79.1	93.5
pill	98.2	99.7	97.9	99.2	84.7	78.8	97.4	99.3	99.9	98.9	99.3	84.2	77.3	97.2
screw	87.5	94.7	90.4	98.9	46.7	53.0	95.5	97.8	99.2	96.7	99.4	55.3	54.1	96.9
tile	99.9	100	98.8	93.9	72.9	67.1	77.5	99.9	100.0	99.4	94.8	74.4	68.1	82.5
toothbrush	98.6	99.5	96.7	98.7	58.2	61.8	93.6	99.4	99.8	98.4	99.2	63.5	65.4	94.8
transistor	99.0	98.4	96.4	87.7	43.1	43.0	82.8	99.7	99.6	97.5	93.7	58.1	56.1	88.7
wood	98.4	99.5	96.8	95.0	70.2	66.0	91.0	99.3	99.8	98.4	95.7	70.9	65.4	91.4
zipper	99.8	100	99.2	98.8	78.9	74.0	95.4	99.9	100.0	99.6	99.1	79.3	74.2	96.8
Mean	97.4	99.0	96.9	96.5	64.2	62.4	90.5	98.7	99.5	97.7	97.7	67.5	64.8	91.9
VisA														
candle	94.8	95.5	89.2	98.6	37.8	41.7	97.1	96.6	97.0	90.9	98.8	39.0	41.8	97.0
capsules	94.8	97.1	92.0	99.8	72.5	72.1	97.8	95.4	97.2	92.3	99.9	71.7	73.5	97.7
cashew	96.2	97.9	95.1	91.9	46.8	50.9	77.9	97.4	98.6	96.6	87.5	45.4	53.8	76.7
chewinggum	98.3	99.3	96.4	98.1	51.7	52.1	60.5	99.2	99.6	97.5	98.2	38.5	45.0	61.4
fryum	97.7	98.9	94.6	97.5	51.4	54.5	94.3	98.3	99.2	94.8	96.8	43.5	47.8	94.8
macaroni1	99.5	99.5	96.6	99.8	30.4	37.0	98.7	99.3	99.2	96.6	99.9	34.6	42.9	98.7
macaroni2	94.2	94.3	88.5	99.8	24.8	31.8	98.8	96.0	96.1	90.2	99.9	28.8	36.5	98.9
pcb1	96.3	95.4	93.1	95.5	26.3	36.2	93.5	97.5	96.4	95.7	95.7	25.1	37.1	94.4
pcb2	98.8	98.7	96.5	97.3	21.2	26.7	90.2	99.0	99.0	97.5	97.7	14.0	22.5	90.2
pcb3	99.3	99.2	97.5	98.6	21.0	32.2	95.7	99.6	99.6	98.0	98.9	21.2	32.1	96.0
pcb4	99.5	99.5	98.0	97.4	49.6	54.0	84.6	99.3	99.2	97.0	97.9	51.4	52.0	86.5
pipe_fryum	98.0	99.0	94.3	99.4	68.6	66.7	94.6	98.6	99.3	95.6	99.3	69.6	65.2	95.1
Mean	97.3	97.9	94.3	97.8	41.9	46.3	90.3	98.0	98.4	95.2	97.5	40.2	45.8	90.6

Table 9: Training-epoch ablation on MVTec-AD. Best values across epochs are shown in **bold**.

Ablation	Epoch	Image-level			Pixel-level			
		AUROC	AP	F1-max	AUROC	AP	F1-max	PRO
<i>Training duration</i>								
	100	91.7	96.4	93.9	95.6	57.3	56.7	87.9
	200	95.3	98.0	95.1	96.2	61.0	60.0	89.4
	300	96.3	98.4	96.1	96.6	63.0	61.6	90.5
	400	96.3	98.5	95.7	96.6	63.7	62.1	90.4
	500	97.4	98.9	96.4	96.9	64.4	62.8	91.0
	600	97.5	98.9	96.6	97.0	64.8	63.0	91.4
	700	97.4	98.9	96.3	97.1	65.3	63.4	91.2
	800	97.8	99.2	96.8	97.4	66.0	63.7	91.4
	900	98.0	99.2	97.0	97.3	65.9	63.6	91.3
	1000	98.0	99.2	97.1	97.3	66.4	64.0	91.1
	1100	98.0	99.2	97.3	97.4	66.3	63.9	91.5
	1200	98.1	99.2	97.1	97.4	66.8	64.3	91.8
	1300	98.2	99.3	97.2	97.6	67.1	64.5	91.4
	1400	98.2	99.3	97.3	97.6	67.0	64.3	91.7
	1500	98.2	99.3	97.3	97.6	67.2	64.6	91.8
	1600	98.4	99.4	97.4	97.5	67.3	64.9	91.8
	1700	98.5	99.4	97.5	97.6	67.2	64.6	91.7
	1800	98.5	99.4	97.6	97.4	67.1	64.3	91.6
	1900	98.5	99.5	97.6	97.6	67.4	64.7	91.8
	2000	98.7	99.5	97.7	97.7	67.5	64.8	91.9

F Qualitative results

We present more qualitative results on VisA and MVTec in Figure 13,14. Our method demonstrates strong localization ability, capable of capturing even the smallest anomaly.

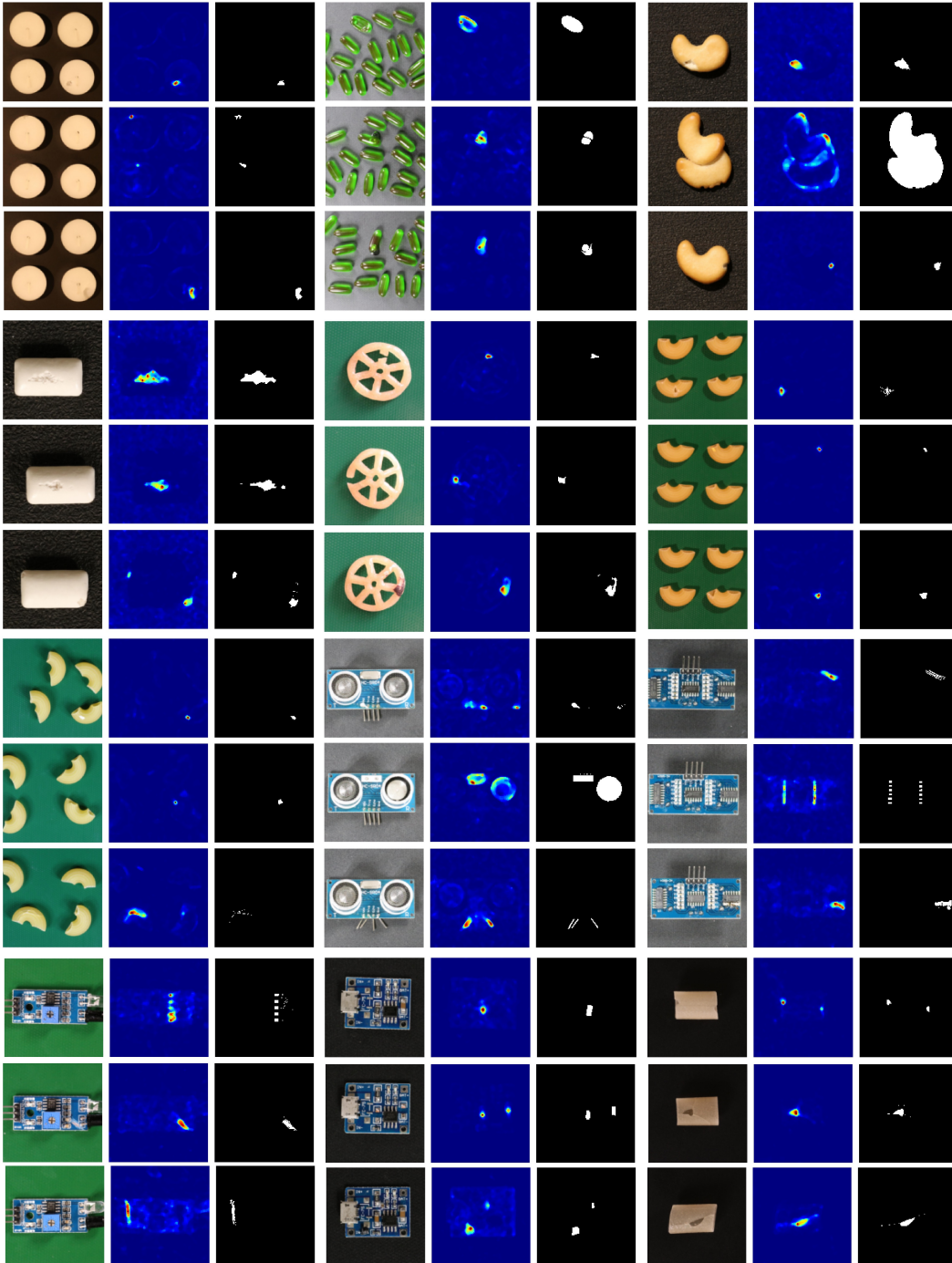


Figure 13: Qualitative results of Flow Mismatching on VisA dataset.

